RESEARCH ARTICLE

Key Points:
- Seismic energy is 10^{-7} to 10^{-4} of impact kinetic energy
- Block volume is best estimated from impact kinetic energy
- The acceleration spectrum centroid frequency of breakage impacts is higher than that of intact blocks

Correspondence to:
L. Saló,
lluissalo@gmail.com

Seismic Energy Analysis as Generated by Impact and Fragmentation of Single-Block Experimental Rockfalls

L. Saló[1,2] , **J. Corominas[1]** , **N. Lantada[1]** , **G. Matas[1]** , **A. Prades[1]** , and **R. Ruiz-Carulla[1]**

[1]Department of Civil and Environmental Engineering, Universitat Politècnica de Catalunya, Barcelona, Spain, [2]Now at Department of Civil and Environmental Engineering, Massachusetts Institute of Technology, Cambridge, MA, USA

Abstract   The analysis of seismic signals obtained from near-source triaxial accelerometer recordings of two sets of single-block rockfall experiments is presented. The tests were carried out under controlled conditions in two quarries in northeastern Spain; in the first test (Foj limestone quarry, Barcelona), 30 blocks were released with masses ranging between 475 and 11,480 kg. The second test (Ponderosa andesite quarry, Tarragona) consisted of the release of 44 blocks with masses from 466 to 13,581 kg. An accelerometer and three high-speed video cameras were deployed, so that the trajectories, velocities, and block fragmentation could be tracked precisely. These data were used to explore the relationship between seismic energy and rockfall kinetics (the latter obtained from video analysis). We determined absolute and relative values of seismic energy and used them to estimate rockfall volumes. Finally, the seismic signature of block fragmentation was assessed in both the frequency and time domains. The ratios of seismic energy after impact to kinetic energy before impact ranged between 10^{-7} and 10^{-4}. These variables were weakly correlated. The use of seismic energy relative to impacting kinetic energy was preferred for the estimation of volumes. Block fragmentation impacts were dominated by higher acceleration spectrum centroid frequencies than those of nonfragmentation impacts: 56.62 ± 2.88 and 48.46 ± 4.39 Hz at Foj and 52.84 ± 12.73 and 38.14 ± 4.73 Hz at Ponderosa.

Plain Language Summary   Gravitational instability movements on mountain slopes are spontaneous in nature. In most cases, continuous seismic recordings are the only available data; thus, inference techniques are used to approximate the initial characteristics of the detached mass. Here we perform two sets of individual rock block release experiments in a highly monitored setting in northeastern Spain; in addition to the seismic instrumentation, a detailed study of block properties and the deployment of video cameras allow an accurate determination of the input parameters (volumes and impacting speeds), which are usually unknown in natural settings. This is used to relate seismic observations to known characteristics of the performed block releases. We find that (1) radiated elastic energies from the point of impact are significantly smaller than the impact energy, regardless of block breakage, (2) the usage of kinetic energy is preferred for the estimation of rockfall volumes, and (3) block fragmentation can be characterized by means of individual parameters associated with the radiated wave frequencies. These results should shed further light on how efficient the conversion of impact to radiated elastic energy is and on the level of inference that can be achieved based on seismic signals.

1. Introduction

Controlling the hazards associated with rockfalls, landslides, and related mass wasting is now an issue of concern. The number of endangered inhabited areas has increased in recent years, mainly due to population and infrastructure growth (e.g., Petley, 2013). In spite of available methods to detect potentially unstable rockfall sources such as satellite image analysis, digital photogrammetry, or terrestrial laser scanning (e.g., Jaboyedoff et al., 2012; Sturzenegger & Stead, 2003), these phenomena are not easy to capture in their natural state. Real-time observations of the failure process are unlikely, owing to the unprompted nature and time span of these events, which usually occur in a matter of seconds.

Continuous seismic recordings can be used to detect and study rockfalls and other mass instabilities and have been found to be a powerful source of information. Studies undertaken to date have been able to detect

and locate events (e.g., Deparis et al., 2008; Hibert et al., 2011, 2014; Lacroix & Helmstetter, 2011; Suriñach et al., 2005), determine associated seismic energies (e.g., Bottelin et al., 2014; Deparis et al., 2008; Hibert et al., 2014; Yamada et al., 2012), and deduce the size, force, and kinetic parameters of large mass movements (e.g., Allstadt, 2013; Ekström & Stark, 2013; Favreau et al., 2010; Hibert et al., 2015; Moretti et al., 2012). Furthermore, short-period (unless otherwise specified, we refer to frequencies in the order of 10^0 Hz or higher when the terms "short period" or "high frequency" are employed in this paper; below 10^0 Hz, "long period" or "low frequency" is used instead) elastic waves carry additional information regarding the source mechanisms and dynamics of failure on rock cliffs and slopes (e.g., Chen et al., 2013; Dammeier et al., 2011, 2016; Deparis et al., 2008; Helmstetter & Garambois, 2010; Vilajosana et al., 2008).

High-frequency signals are less stable (with increased attenuation, dispersion, and spreading), but they can be observed for smaller events. Owing to the increasing density of regional and local seismic networks, the analysis of high-frequency seismic signals to infer multiple characteristics of mass movements has augmented in recent years: the volume of the detached mass has been related to both seismic amplitude and energy (Dammeier et al., 2011; Hibert et al., 2011; Norris, 1994; Yamada et al., 2012), momentum to signal envelope and amplitude (Hibert, Ekström, & Stark, 2017; Schneider et al., 2010), and modeled force to signal power (Levy et al., 2015). In contrast to studies based on longer-period waves, the aforementioned studies have shown that short-period waves may be used directly from recordings (without inversion) to quantify kinetic parameters; this could have direct applications in real-time monitoring.

Human-triggered events subject to enhanced monitoring have provided additional information about seismic signals associated with rockfalls. Vilajosana et al. (2008) found that rockfall impacts on the ground produced strong, linearly polarized waves that can be used to locate events if at least two recording stations are available. Moreover, impacts were characterized by an impulsive signature that was present in the entire frequency band of the analyzed spectra (up to 50 Hz). In a similar rockfall context, Bottelin et al. (2014) reported that seismic phases can be differentiated by using video and seismic signal recordings simultaneously, and both Vilajosana et al. (2008) and Bottelin et al. (2014) showed that the most energetic phases relate to specific impacts after a free-fall section.

Questions yet to solve in the context of seismic signals generated by rockfalls include the understanding of high-frequency sources (relative to the observed frequency band) and the relation between propagating projectile dynamics and their associated vibration. Previous studies have already considered field experiments to enhance the interpretation of seismic signal recordings. Field tests conducted by Huang et al. (2007) focused on the relationship between recorded signals resulting from individual impacts and those of debris flows. The similarities in their results point to interactions between the ground and individual rocks that dominate recorded vibrations in these flows. In a study comprising both theory and experiments, Farin et al. (2015) established relations between the frequency-dependent elastic energy and mass and velocity of the impacting body; however, the inference of both parameters from seismic energy did not provide positive results in field conditions. Additionally, a recent study by Hibert, Malet, et al. (2017) explored both seismic amplitude and energy in relation to the kinetics of impacts. The authors used a similar experiment to ours in which 28 blocks were released in a marl gully. They found first-order polynomial scaling relationships between kinetic parameters, recorded amplitudes, and seismic energy. They utilized their correlation equations to infer the mass and velocity of impacts, with reasonably good results. Open queries that naturally emerge from these studies concern the control of terrain properties and block size in the scaling relationships. Moreover, Hibert, Malet, et al. (2017) note that attenuation models need be ameliorated to reduce uncertainties.

We performed two controlled experiments with a total of 74 single-block releases at two different quarries in Catalonia, Spain (Figure 1). The first experiment was conducted at Foj quarry (41.361°N, 1.923°E), and the second at Ponderosa quarry (41.163°N, 0.943°E). Both tests were carried out in the framework of the project RockRisk (Corominas et al., 2017), an important part of which has been dedicated to determining fragmentation of rock masses and its application in fragmentation and propagation models (Matas et al., 2016, 2017; Ruiz-Carulla et al., 2015, 2016). In this study, we concentrated on the emitted seismic energy values and time (t)-frequency (f) features of recorded signals and compared them to free-fall kinetics and fragmentation, respectively. We aimed to (i) determine absolute and relative values of radiated elastic energy (throughout the paper, we indistinctly refer to seismic energy as either seismic energy or radiated elastic energy) as generated by the impacts of controlled and highly monitored single-block rockfalls, (ii) infer block volumes from the ratios obtained between seismic energy (E_s) and both kinetic (E_k) and potential (E_p) energy, and (iii) explore
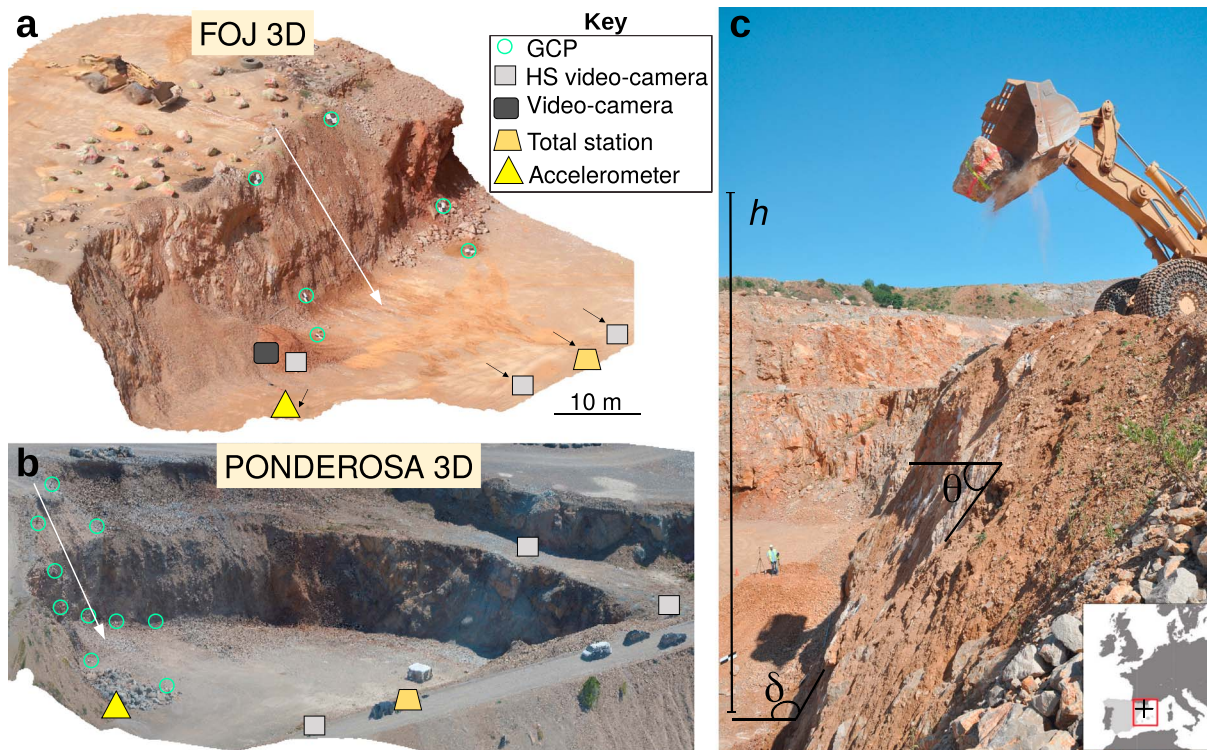
Figure 1. (a, b) Images of the 3-D models of the testing sites, showing the position of instrumentation. Devices signaled with an arrow were placed in the indicated direction, some steps behind (out of the modeled area). The white arrows indicate the profile section where the block falls took place. The scale is approximate. (c) Lateral view of the profile at Foj, indicating the total fall height (h), the slope angle (θ), and the considered angle between the deposit and the slope for the volume calculations (δ), according to explanations given in section 3.2 (the same metrics apply to Ponderosa). Note that the testing sites are composed of (i) the slope where the fall propagates and (ii) the quarry floor where the main impact of the block takes place and where the motion of the blocks stops. A small map to contextualize the experiments on a regional scale is also plotted (coordinates provided in section 1). GCP = ground control point.

the seismic signature of fragmentation impacts to characterize the process of breakage in the frequency and time domains. Hence, this paper should shed light on the contribution of seismic energy to energy dissipation by the block impact on the ground, therefore exposing the efficiency of the conversion from kinetic to seismic energy. We also intended to answer whether the breakage of blocks influenced our results and to detail the expression of fragmentation in the recorded seismic signal.

The testing sites consisted of a slope and a horizontal platform (hereafter referred to as the quarry floor) where the main block impact took place and were equipped with a triaxial accelerometer, three high-speed video cameras (HSVCs), two standard high-definition cameras, and ground control points (GCPs). The blocks impacted on the quarry floor at a distance ranging between 20 and 30 m from the accelerometer. In order to construct 3-D models of the two sites, pictures were taken from the ground and from drones (Figure 1). Supervised processing of video frames revealed the block trajectories in space, so the velocities and kinetic parameters could be determined (see section 2.2).

2. Methods

This section first describes the procedures used in the seismic data processing and analysis (section 2.1), which involves the computation of seismic energies and a detailed study of the signature of the fragmentation on seismic recordings. Second, the settings, instrumentation, and methodology for determining block volumes, impacting velocities, and other kinetic parameters are provided (section 2.2). Throughout the text, F is used to refer to fragmented blocks/fragmentation impacts, and NF for cases without fragmentation.

2.1. Seismic Data Processing and Analysis
A manual procedure was used to classify signals from the continuous accelerometric record resulting from each of the two field tests. For each blockfall, two data archives were kept (Figure 2): (1) corresponded to the complete fall (which encompassed all seismic features recorded from when the block was dropped
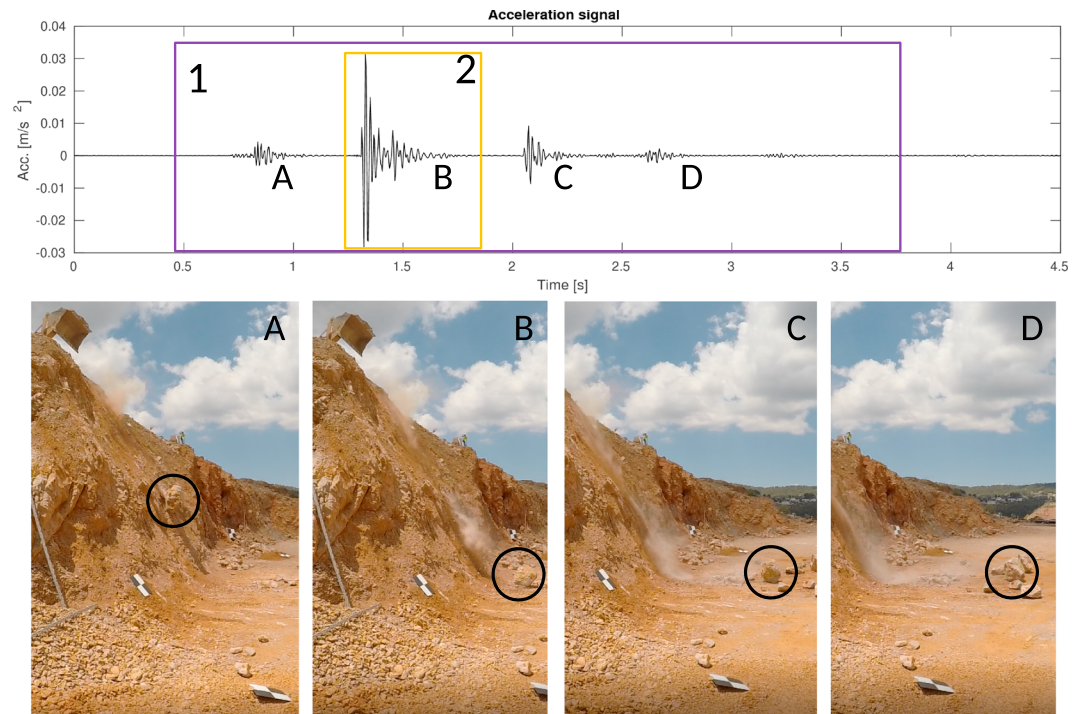
Figure 2. Example of a recorded accelerogram (Block 4 at Foj). For each impact, two recordings were kept: the entire signal (1, purple area) and the waveform corresponding to the main impact on the quarry floor (2, orange area). Impact identification was made by comparison with video camera images. See explanations in sections 2.1 and 2.2.

from the blade until its motion stopped) and (2) included only the waveform of the main impact on the quarry floor. This was done because two values of seismic energy were computed for each block: one for the entire signal from (1, E_{sT}) and one for the main impact from (2, E_s). The first value was only used for comparison to E_p (total energy of the blockfall process), while E_s was used elsewhere. When either of the two apply (e.g., in equation (1) and section 2.1.1), the term $E_{s(T)}$ or just E_s is used.

An initial spectrogram evaluation of the raw signals was performed to examine the frequency band in which most of the energy was found. This preliminary analysis was focused on waveform-spectrogram comparison near the peak ground acceleration (PGA) occurrence (Figure 3). With a sampling frequency of 250 Hz, the Nyquist frequency for our recordings was 125 Hz (i.e., the maximum observable frequency). Qualitative observation of spectrograms revealed dominant frequencies of around 50 Hz, although energy could be seen in most of the shown frequency band. To preserve all observed energetic frequencies, signals were filtered between 5 and 120 Hz for the entire analysis. The signals displayed clear onsets of waves and almost no background power before their arrival (Figure 3). This observation was supported quantitatively by a mean noise energy calculation before the impacts and within this frequency band. Noise energy values were found to be insignificant (see section 3.1); thus, we did not perform any further processing to eliminate background noise.

The performed seismic signal analysis excluded a few recordings with a much weaker waveform expression and recordings of blocks that fragmented on the slope (before the main ground impact). The first discarded group included some blocks with small volumes ($V < 0.4$ m^3; refer to Table A1 for the volume range of the selected blocks). Although most of the selected blocks were larger, not all of them were, so this reasoning cannot justify the weaker signals; however, no alternative satisfactory explanation could be found for this reduced expression in some signals. Regarding the second discarded group, as both seismic energy (E_s) and fragmentation are explored hereafter, including them would have resulted in two different seismic signals (that of the main impact for E_s, as explained above, and that of the breakage impact on the slope for F) being used for the same block release. Fragmentation on the slope only occurred for four blocks at Foj quarry and one at Ponderosa, so these blocks were removed to avoid confusion. After the selection process, the total number of blocks used (and their associated seismic signals) in this article is 21 for the Foj data set and 28
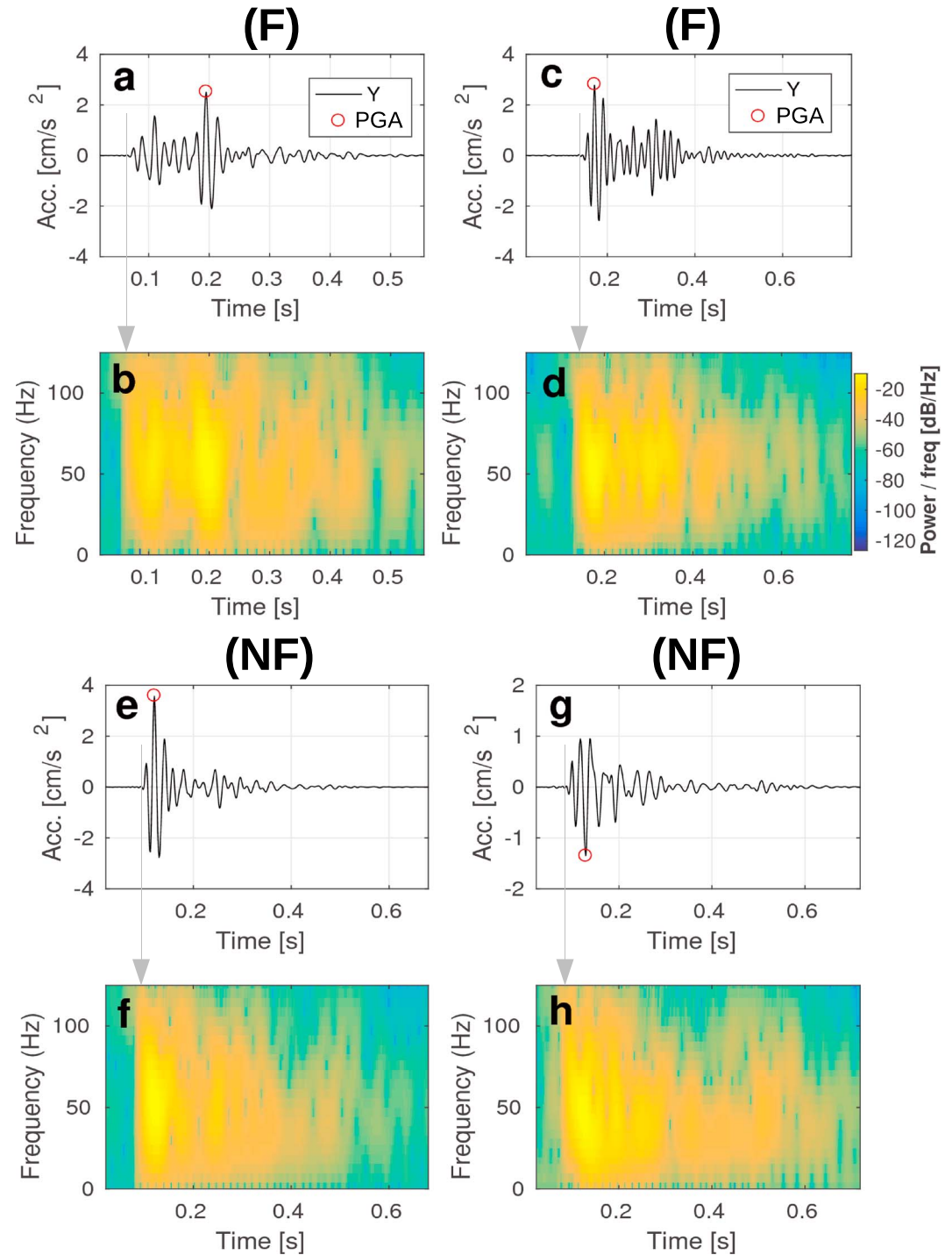
Figure 3. Accelerograms (a, c, e, and g) and acceleration spectrograms (b, d, f, and h) corresponding to the main ground impact of Blocks 1, 3 (F) and 4, 9 (NF) at the Foj test site. Each block has its own pair (e.g., a and b for Block 1, and c and d for Block 3), and arrows are provided to help correlate the start times of the signal and the energy displayed in the spectrograms. The most energetic frequencies were those around 50 Hz (slightly higher for F impacts), although the frequency band 5–120 Hz was filled to some extent for most of the impacts. The spectrograms were calculated with a moving window of length ~10% that of the signal and ~90% of overlap. They present the power spectral density relative to the shown frequencies over time and are reported in decibel as follows: Amplitude (dB) = $10\log_{10}$(power spectral density). In addition, no filtering is applied before displaying the spectrograms, because they were used as a tool for deciding which passband should be kept. PGA = peak ground acceleration.

for the Ponderosa data set. All blocks within the selected group that fragmented did so on their first impact on the quarry floor (Figure 1 and Table A2).

2.1.1. Radiated Elastic Energy Estimation

In seismology, the quantification of energy radiated from the source (an earthquake) through a solid medium has long been addressed (Lamb, 1904). Rockfalls and landslides are found among other natural sources that release energy that propagates in the form of elastic waves. To date, various methods have been proposed for estimating the energy radiated from the source in rockfalls, landslides, and related phenomena. Previous studies in this context have used formulas initially derived for earthquakes, in which the seismic energy is computed from the magnitude following Kanamori's (1977) relation (Bottelin et al., 2014; Deparis et al., 2008; Weichert et al., 1994) or, as reported in Farin et al. (2016), have integrated the flux of energy that is transmitted 360° from the source across a solid layer (Farin et al., 2015; Hibert et al., 2011, 2014; Hibert, Malet, et al., 2017; Levy et al., 2015; Vilajosana et al., 2008). For the latter (henceforth called the flux method), a different expression needs to be used depending on whether internal (e.g., Vilajosana et al., 2008) or surface waves (e.g., Hibert et al., 2011; Vilajosana et al., 2007) dominate the seismic signal. Additionally, the flux method assumes a point-force source and an isotropic homogeneous medium (Dahlen, 1993; Kanamori & Given, 1982).

We use the flux method to compute the seismic energy ($E_{s(T)}$) generated by each block (equation (1)). Appendix B reports the results of a quantitative three-component wave polarization analysis based on Vidale (1986), from which we conclude that surface waves dominate the recorded signals. Second, we consider the supposition of a point-force source to be realistic enough in our context of single-block impacts. This has long been documented to fit shallow landslide sources (e.g., Dahlen, 1993; Eissler & Kanamori, 1987; Kanamori & Given, 1982; Kawakatsu, 1989) and is also supported by the fact that the flux method has been recurrently used in papers exploring rockfall seismic signals (e.g., Hibert et al., 2011; Vilajosana et al., 2008). The accuracy of the required isotropic homogeneous medium assumption is more difficult to quantify, given that detailed geotechnical data on the bedrock were not acquired. Each substrate was lithologically constant (the same unit was found throughout the region of interest in the quarry). However, they were filled with a thin layer of rock debris of irregular thickness, and both the fracture pattern and the joint spacing (as observed in the outcrops) showed spatial variability; this led to an undetermined level of ground heterogeneity, even in the controlled conditions of our field tests (section 2.2). Discontinuities influence wave propagation in terms of attenuation, velocity, and shear wave splitting. Hence, some scatter in our seismic energy results may have been caused by this fact, which is acknowledged in the discussion (see section 3.1).

As explained above, signals were filtered from 5 to 120 Hz using a third-order Butterworth filter, to ensure the inclusion of all observed energetic frequencies in the analysis (Figure 3). While this passband managed to capture all observed frequencies that are relevant, it did not define the full frequency range of the impact process. Appendix C provides the theoretical spectral velocity peaks at the impact point, computed by applying the Hertz impact theory as in McLaskey and Glaser (2010). The results show that the energy of the spectral peaks above 120 Hz only represents, in nearly all cases, 2.4% or less of the energy in the frequency band that we captured. Thus, the employed frequency range for the seismic energy computation allows a reliable estimate.

$$E_{s(T)} = \int_{t_i}^{t_f} 2\pi r h_R \rho c_R u_{\text{env}}(t)^2 e^{\alpha r} \, dt \tag{1}$$

$$H_I(t) = \int_{t=0}^{t=\text{final}} a(t)^2 \, dt \tag{2}$$

$$u_{\text{env},i}(t) = \sqrt{u_i(t)^2 + H_t(u_i(t))^2} \tag{3}$$

In equation (1), t_i and t_f represent the onset and final times of the waveform, which we obtained as those corresponding to the 0.05 and 99.95% limits of the Husid integral ($H_I(t)$), namely, the cumulative integral of the squared acceleration as shown in equation (2) (e.g., Boore & Thompson, 2014). In our case, this criterion allows reliable identification of the initial and end times of the relevant part of the waveform. While a wave arrival picking algorithm could have been used instead, it would have been computationally more expensive and the variations in the obtained seismic energy values would have been nearly nonexistent. This was affirmed after a comparison of E_s values for two signals whose start and end times were also picked manually. Furthermore, seismic energies were, essentially, the result of the main waves in each waveform, which were

neither at the exact beginning or end of the signal. r is the distance source (event)-receiver (accelerometer), of some 20–30 m for our impacts, h_R is the significant layer thickness for surface waves, ρ is the ground density, c_R is the phase velocity of seismic surface waves, $u_{env}(t)$ is the amplitude envelope of ground velocity (which requires the integration of the acceleration signal) obtained by using the Hilbert transform (H_t) as shown in equation (3). For each of the three spatial components, an envelope was obtained as in equation (3), and then we obtained the total envelope (which was ultimately used to compute $E_{s(T)}$) by vectorial composition of the other three as $u_{env}(t) = \sqrt{u_{env,x}(t)^2 + u_{env,y}(t)^2 + u_{env,z}(t)^2}$. Depending on whether E_s or E_{sT} was calculated, the input data archive contained the total number of recorded impacts or only the main one (Figure 2), and so t_i, t_f, and $u_{env}(t)$ changed accordingly for each computation. α is the frequency-dependent damping factor introducing inelastic attenuation of surface waves (Aki & Richards, 1980), calculated as in equation (4).

$$\alpha = \frac{f_{CTR}\pi}{Qc_R} \tag{4}$$

$$f_{CTR} = \frac{\sum_{f=5}^{f=120} f \cdot y(f)}{\sum_{f=5}^{f=120} y(f)}. \tag{5}$$

In this case, we employ the frequency centroid (f_{CTR}) of the acceleration spectrum, computed as in equation (5), where $y(f)$ is the numerical spectrum amplitude value associated with an f value (L/t units) and f the frequency. We relied on the fact that f_{CTR} represents the mass center where most of the energy is found, and we used the f_{CTR} value obtained for the main impact (where most of the seismic energy is released) for both E_{sT} and E_s. We also used the f_{CTR} to determine h_R as $\frac{1}{4}\lambda$, where $\lambda = c_R/f_{CTR}$ is the wavelength (Aki & Richards, 1980; Vilajosana et al., 2007). As indicated in Table A1, the ground densities (ρ) were assumed to be 2,500 kg/m³ at Foj quarry and 2,700 at Ponderosa, which are classic values for limestone and andesite rocks. The seismic phase velocity of surface waves (c_R), in m/s, was calculated to be 1,690 at Foj and 2,200 at Ponderosa. To obtain c_R, we used reported values for shear wave speeds (β) in limestone and igneous rocks (Assefa et al., 2003; Simmons, 1964) and followed Stein and Wysession (2003) to ascertain their velocity as $(2 - 2/\sqrt{3})\beta$, considering Rayleigh waves to be representative of the recorded signals (see Appendix B). Q is the dimensionless quality factor accounting for the attenuation of a seismic wave (Xia et al., 2002) and is set to 10, which stands for a moderately damaged medium (e.g., Farin et al., 2015). Even though the previous assumptions are reasonable, neither Q, c_R nor the terrain's ρ could be very well constrained (i.e., no quantification was made from field data). To consider this uncertainty, we also performed a computation based on 1,000 realizations in which their values were varied within a likely span. The goal was to limit uncertainty by observing maximum potential deviation from our best estimate (BE) of values reported above. Ranges were selected according to geologic setting and obtained/chosen values in the previous literature (Farin et al., 2015; Hibert et al., 2011, 2014; Vilajosana et al., 2008; Xia et al., 2002) and were as follows (further explanation is provided in the next paragraph): $800 \leq c_R \leq 2,000$ (m/s) and $1,900 \leq \rho \leq 2,600$ (kg/m³; Foj), $900 \leq c_R \leq 2,200$ and $2,100 \leq \rho \leq 2,800$ (Ponderosa); $3 \leq Q \leq 30$. Each of the 1,000 computations picks a random value within the specified ranges for the previous three parameters. All range values for a certain parameter had equal probability of being selected.

Previous papers computing radiated elastic energies determined phase velocities from standard phase picking as in Vilajosana et al. (2008) or from geophysical methods (e.g., Hibert, Malet, et al., 2017 based on Hibert et al., 2012). Seismic wave propagation time could not be used here to determine c_R, because the accelerometer and cameras were not set to the same time systems (refer to section 2.2.2 below). Thus, a theoretical approach in which c_R was estimated from shear wave speeds was used. Because previous studies obtained lower values than ours (in the range of 300–1,000 m/s), the BEs computed for c_R herein lie in the upper extreme of the considered range. The computation of α following equation (4) involved both c_R and a dimensionless quality factor Q. The latter appears to range from close to 1 (*very damaged medium*) to 30 (*slightly damaged*) in most literature references (Farin et al., 2015; Hibert et al., 2011, 2014; Vilajosana et al., 2008; Xia et al., 2002). We excluded from this span the most extreme values of $Q < 3$ only, relying on the fact that for our case, the medium could range from almost intact to somewhat damaged. Ground densities ρ have previously been selected either by choosing common values in the literature for a certain terrain type (e.g., Hibert et al., 2011, 2014) or by comparing phase velocity values that were obtained with those expected for different rock densities (Vilajosana et al., 2008). Here we assumed that quarry rock densities apply.

While the boundary conditions for the calculation and comparison of seismic energy values were very well constrained (see section 2.2), it should be noted that the use of only one recording device limited

the maximum level of inference based on seismic signals. Detection of local terrain heterogeneities in a particular direction, determination of phase velocities by using travel time residuals, and computation of a local attenuation relationship (and α) are aspects that are outside the scope of this study, due to network shortcomings.

2.1.2. Characterization of the Fragmentation Seismic Signature

In rockfalls, fragmentation analysis is still in its early phase (Arosio et al., 2015; Giacomini et al., 2009; Ruiz-Carulla et al., 2016). However, an improved understanding of this phenomenon is required to improve its prediction and consequences. Rockfalls have two phases in which fragmentation is of paramount importance: the beginning (detachment of the rock mass from the cliff) and the impact of the block(s) on the ground. Seismic signal recordings of crack propagation have been studied in the context of freeze-thaw cycles (e.g., Amitrano et al., 2010) and stress loading (e.g., Senfaute et al., 2009; Spillmann et al., 2007; Walter et al., 2012) with a concern for the initiation of the main instability movement. The aforementioned literature shows that precursory signals can be detected (see also Arosio et al., 2015, and references therein, for an extended background). Nevertheless, to our knowledge, extensive seismic signal analysis of rockfall block breakage upon impact has not been conducted so far.

Herein, we focus on determining which seismic signal features that are systematic of fragmentation impacts were recorded by the accelerometer and explore them in the frequency and time domains. Consequently, the seismic recordings that correspond to the main impact on the quarry floor are used for this part (Figure 2). The frequency parameters listed below were chosen to quantify the differences observed qualitatively in a preliminary revision of the first recordings at Foj quarry (Figures 3 and 4). It was first noticed that recorded frequencies were higher and spectra sometimes showed a dominant and sharp peak when block breakage took place. Conversely, no evidence of fragmentation in time domain was found from these initial observations. Therefore, time parameters were picked to provide information about the signal's duration and increasing time, intensity, and impulsiveness (Figure 5), to acquire a thorough characterization of the seismic signal. If fragmentation is linked to any characteristic in the time domain, then it should most likely respond to duration, intensity of the impact, or emergence of the signal, and so this characterization could be able to capture it. In addition, all F and NF spectra and signal envelopes and their stacks (mean) were studied together to complete this part. To avoid digital integration, the analysis was performed directly on the acceleration signals, which were band-pass filtered from 5 to 120 Hz as noted above. Because we emphasize the comparison between F and NF recordings, it should be noted that choosing of a particular criterion for determining a parameter is not as important as maintaining the same criterion for all studied recordings (i.e., we are more interested in the relative variations observed between F and NF blocks than in the absolute values themselves). For parameter computations, the initial and final times correspond to those selected for the calculation of E_s (t_i and t_f; obtained as detailed above following equation (1):

i. *Predominant frequency f_p*. The predominant frequency is defined as that corresponding to the maximum value y_{max} of the discrete acceleration spectrum y, of a block impact, that is, the X coordinate associated with y_{max}. Spectra are obtained with a fast Fourier transform (FFT) algorithm (e.g., Figure 4).

ii. *Frequency (or spectral) centroid f_{CTR}*. While some spectra show a dominant peak, others have multiple peaks and are not centered around the main one. The frequency centroid is a measure of where (i.e., at which frequency) their center of mass is located and thus supplies additional information for the latter cases that the f_p cannot provide. Using frequency and amplitude information from the FFT computation, f_{CTR} is evaluated as in equation (5) above. In the key points, abstract, and conclusions, we use the equivalent terms *spectral centroid frequency* or *acceleration spectrum centroid frequency*, to emphasize that this is a measure of the frequency (and not amplitude) and that it is measured from the acceleration spectra.

iii. *Bandwidth BW*. This parameter is intended to characterize the sharpness of the main spectral peak, which was seen to vary substantially. Scanning each discrete spectrum from the predominant frequency, we compute the difference between the highest (f_f) and lowest frequencies (f_i) whose associated values $y(f)$ are still larger than $y_{max} / \sqrt{2}$, which corresponds to a loss of 3 dB in amplitude (approximately a 30% decrease). Thus, the BW of a spectrum (equation (6)) diminishes with increased sharpness of the main peak:

$$BW = f_f - f_i. \tag{6}$$

The threshold value of a 3-dB loss in amplitude was picked to ensure that (i) the energy decay was already significant and (ii) the value was not too large so that the algorithm, which searched the nearest sample to that of the decay amplitude, found it within the main spectral peak.
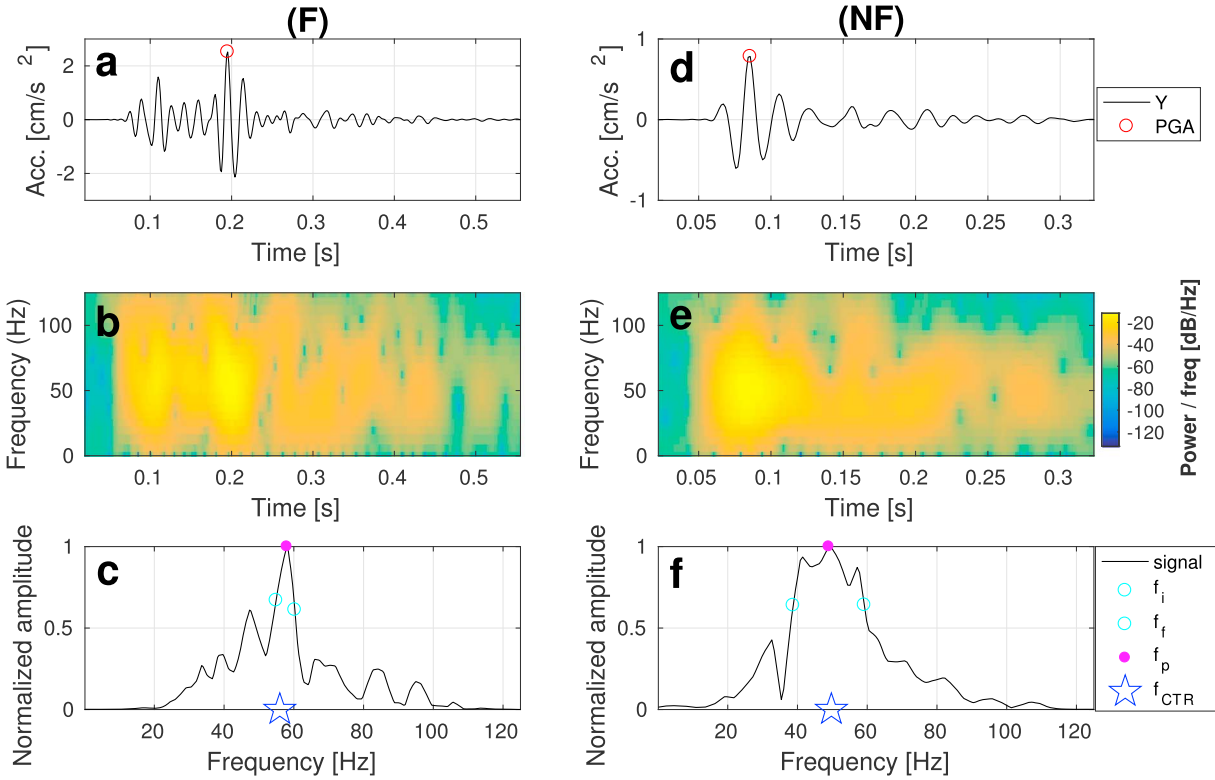
Figure 4. Accelerogram, acceleration spectrogram, and acceleration spectrum (top to bottom) of a fragmentation (a–c) and nonfragmentation (d–f) impact, both recorded at Foj (Blocks 1 and 7, respectively). The signal and spectra (panels a, d and c, f) were filtered between 5 and 120 Hz. The spectrograms were calculated with a moving window of length ~10% that of the signal and ~90% of overlap. We show the power spectral density relative to the plotted frequencies over time (raw signal) and report it in decibel as follows: Amplitude (dB) = $10\log_{10}$(power spectral density). Central panels: Note that the left-side spectrogram is centered at higher frequencies than the one to its right. Lower panels: Spectral centroid f_{CTR}, predominant frequency f_p, and bandwidth (represented here using initial and final points f_i and f_f). Single-sided spectra were computed using a fast Fourier transform algorithm and amplitudes were normalized to the maximum. See text in section 2.1.2 for descriptions of parameter calculations. PGA = peak ground acceleration.

iv. *Bounded duration of an impact signal BD.* The impact duration (equation (7)) is evaluated here as the time span between the first (t_i) and last (t_f) sample inside the 0.05 and 99.95% limits of the Husid integral $H_I(t$; see equation (2)).

$$BD = t_f - t_i. \tag{7}$$

v. *Increasing and decreasing phase ratio ID.* We considered whether fragmentation of a block on ground impact influences the emergence of the signal. We address this issue by dividing the duration of the rise time by that of the decreasing time. This parameter was previously used by Hibert et al. (2014; in velocigrams) to differentiate between rockfall seismic signals and volcano-tectonic tremors. It is quantified as in equation (8), where PGA is the peak ground acceleration:

$$ID = \frac{t_{PGA} - t_i}{t_f - t_{PGA}}. \tag{8}$$

vi. *Arias intensity I_A.* Threshold values for landslide triggering have been previously defined by using the Arias intensity (e.g., Bommer & Boore, 2004). Here we include this parameter to study whether fragmentation impacts are related with (i.e., generate) systematically higher intensities of vibration. It is computed as expressed in equation (9):

$$I_A = \frac{\pi}{2g} \int_{t_{iA}}^{t_{fA}} a(t)^2 dt \quad (m/s), \tag{9}$$
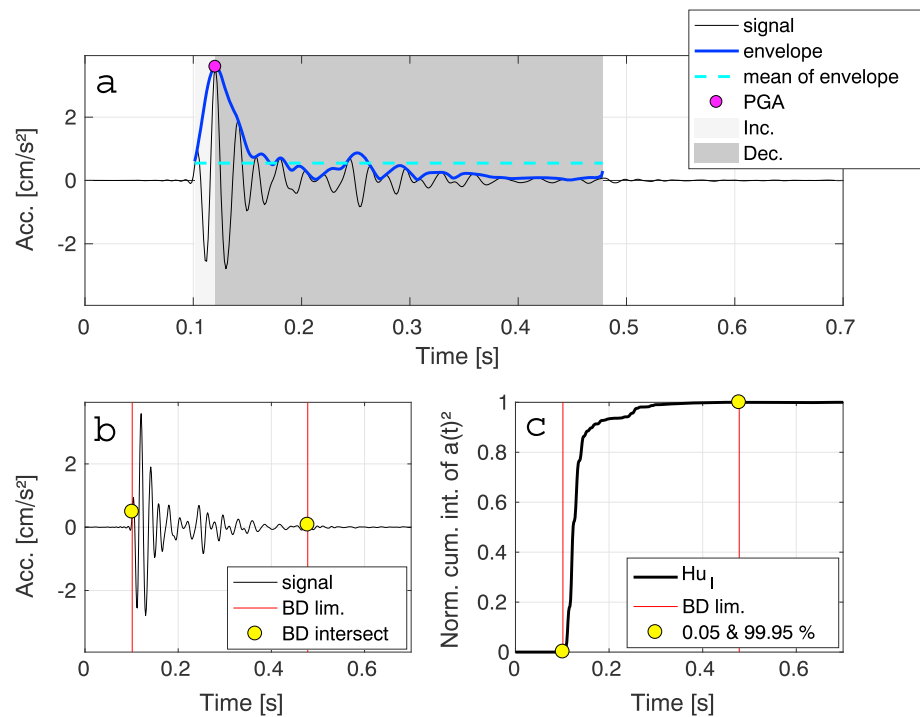
Figure 5. Time analysis of Block 4 at Foj. (a) Acceleration signal and amplitude envelope (computed as in equation (3)), its mean, peak ground acceleration (PGA), and duration of increasing and decreasing phases for the computation of increasing and decreasing phase ratio (shaded in gray according to the legend). (b) Acceleration signal and bounded duration limits. (c) Husid plot showing the cumulative integral of the squared acceleration and its 0.05% and 99.95% values, which were used throughout the paper to determine signal duration. The integral is normalized to the maximum value.

where t_{iA} and t_{fA} are the lower and upper time values limiting the strong vibration phase (Arias, 1970). For convenience, we ascribe $t_i = t_{iA}$ and $t_f = t_{fA}$. $a(t)$ is the acceleration signal, and g is the gravitational acceleration (9.81 m/s^2).

vii. *Ratio of the PGA to the envelope mean R_{pem}.* This parameter is intended to differentiate signals with a well-defined peak from others that are rather flat throughout their duration, as previously done by Hibert et al. (2014). We compute the PGA and envelope mean of the acceleration signal. The mean is taken from the amplitude envelope obtained as in equation (3), which covers the absolute value of the signal.

Figures 4 and 5 illustrate the described parameters to assess the fragmentation signature in the time and frequency domains.

The aforementioned parameters had the best capabilities for characterizing block fragmentation and the seismic signal itself. Additional tested parameters that did not improve the results presented in section 3.3 are listed below. In the frequency domain (acceleration spectrum): peak value, ratio of the energy higher than f_p or f_{CTR} to that lower than f_p or f_{CTR}, energy in the lower portion (up to 10 and 30 Hz) and in the frequency band from 1 Hz to f_p or f_{CTR}, energy in the upper portion (from 70 and 100 Hz to Nyquist frequency), and from f_p or f_{CTR} to Nyquist frequency, BW (in Hz) as explained in (iii.) above for a loss of 40% in amplitude, and ratio of the main to the second peak (this last parameter was found to be higher for most fragmentation impacts at Foj, but not at Ponderosa). In the time domain (acceleration signal): PGA, bounded duration to 10% of the PGA (i.e., the time span between the first and last sample that achieved the indicated threshold value), the envelope mean itself, and the kurtosis and skewness of the envelope (statistical tools to assess how prone to outliers a particular distribution is, and its asymmetry with regard to the mean, respectively). Finally, it should be noted that trials for the parameter computations explained above were carried out using the horizontal (longitudinal and transverse) and vertical components. However, because similar capabilities were found among them (similar results), we only report our findings for the maximum component (the longitudinal) in the results section.

2.2. Experimental Single-Block Rockfalls

2.2.1. Test Site Design and Experiment Description

As fragmentation and rockfall kinetics were to be studied during the tests, the sites were carefully selected to (1) provide enough height gap for impacting energies to be potentially damaging for each block's integrity and (2) allow full instrumentation deployment. Each block was dropped using a bulldozer as a block-picking means, which required wide access to the top of the slope. Both sections were single benched profiles (i.e., a single, continuous slope and the quarry floor). The testing profiles had an upper section with a slightly gentler inclination than the lower one, which was useful to ensure block contact with the slope and increased kinetic energy upon ground impact. For the calculations in section 3.2 below, the mean slope angle (θ) between the crest and the toe is taken. The total fall height (h), including the bulldozer blade, was 16.5 at Foj and 21.5 m at Ponderosa (Figures 1a–1c; the relative location of the deployed instrumentation is provided in the figure as well). The blocks were painted with three main color stripes around each major axis to make them more visible as they propagated down the slope. The deposition floor was cleaned after every ~10 block releases at Foj and ~15 block releases at Ponderosa. The tests consisted of a repetitive process in which each single block was released one by one and tracked by the previously distributed instrumentation. At Foj, the number of impacts on the slope (before the main one on the quarry floor below) was 1 or 2, whereas at Ponderosa it was always 1. See Gili et al. (2016) for further details on the experiment itself.

2.2.2. Instrumentation

A TITAN triaxial accelerometer was placed on the quarry floor, fixed on solid rock at some ~20–30 m from the block impacts on the ground (Figure 1). It was set to a sampling frequency of 250 Hz and to 1/8-g saturation limits to improve its sensitivity.

Four surveying rods and a minimum of six targets (GCPs) were strategically placed around the site to subsequently georeference all images. The video camera set composed of three high-speed video cameras (HSVCs) fixed at a particular position and two standard picture or video digital devices. The cameras were manually initialized at the beginning of each test fall and could be synchronized with each other by means of a photographic flash pulse that was generated three times per block release (just before the drop, during propagation, and near the end time). Unfortunately, because the cameras and accelerometer could not be synchronized, wave propagation times could not be used to infer seismic phase velocities (c_R; see section 2.1.1). In addition, a Leica TM30 reflectorless total station and Unmanned Aerial Vehicle (UAV) aerial photography were used extensively during the tests, to measure positions of GCPs, cameras, and the main fragments' final position (to compute runouts), and to generate orthophotomaps and 3-D models of the testing sites (Prades et al., 2017; see Figure 1).

2.2.3. Block Description, Volumes, and Fragmentation

The bedrock in the two quarries from which the blocks were extracted is used as riprap, to armor shorelines and related structures. The blocks themselves were extracted by blasting from the same lithological unit at each quarry and were provided to us by the operators. They were angular to subangular, and a few of them were subrounded. Similar in size (see Table A1) and appearance (Gili et al., 2016), they can be considered homogeneous when compared to natural rockfall size distributions. Still, Schmidt L-hammer rebound values were not equal for all of them. No correlation was found between block breakage levels and the values provided by the Schmidt L-hammer rebound test, possibly because this method only captures the properties of the block surface (Gili et al., 2017, 2016).

The volume of each block was measured before the experiments. A first approximation was obtained via measuring tape along the three dimensions of the block (V_1). In addition, a photogrammetric survey was employed in situ, to create a 3-D model of each block from which a more accurate volume was later obtained (V_{3D}). The V_{3D} value is used hereafter when referring to the measured volume without further specification. Because the blocks were extracted from rock outcrops at each quarry, the masses (m) were calculated using the exploited rock's density (ρ). Note that the same ρ is used for both the blocks and the terrain, because the blocks were extracted from within the quarry. Table A1 summarizes the results (tables and figures herein report values for the blocks that were studied only. The selection criteria are provided above in section 2.1.).

After each release, two criteria were considered to determine fragmentation (F) of test blocks. The number of generated fragments (N_{frag}) as manually measured on the deposition area was employed in the first defined criterion (F occurs if $N_{frag} > 1$ after impact). However, the fragmented fraction in terms of volume was also considered (F occurs if $V_{final}/V_{initial} < 0.95$ after impact, where V_{final} refers to the volume of the largest individual portion of a block after the impact; the fragmented fraction V_{frag} is then $1 - V_{final}/V_{initial}$, so we are interested

Table 1
Kinetic Parameters and Potential Energies for the Studied Blocks

			Foj						Ponderosa		
No.	m (kg)	v (m/s)	P (kg · m/s)	E_k (J)	E_p (J)	No.	m (kg)	v (m/s)	P (kg · m/s)	E_k (J)	E_p (J)
1	3,114	15.22	4.7E+04	3.6E+05	5.0E+05	1	3,556	17.62	6.3E+04	5.5E+05	7.5E+05
2	2,113	13.11	2.8E+04	1.8E+05	3.4E+05	2	2,025	17.79	3.6E+04	3.2E+05	4.3E+05
3	2,050	14.53	3.0E+04	2.2E+05	3.3E+05	3	1,131	17.03	1.9E+04	1.6E+05	2.4E+05
4	2,959	14.33	4.2E+04	3.0E+05	4.8E+05	4	1,655	18.08	3.0E+04	2.7E+05	3.5E+05
5	4,774	14.59	7.0E+04	5.1E+05	7.7E+05	5	1,069	17.92	1.9E+04	1.7E+05	2.3E+05
6	2,027	12.67	2.6E+04	1.6E+05	3.3E+05	6	1,884	18.50	3.5E+04	3.2E+05	4.0E+05
7	1,592	14.31	2.3E+04	1.6E+05	2.6E+05	7	3,308	16.92	5.6E+04	4.7E+05	7.0E+05
8	2,508	14.68	3.7E+04	2.7E+05	4.1E+05	8	13,581	17.30	2.3E+05	2.0E+06	2.9E+06
9	2,253	13.76	3.1E+04	2.1E+05	3.6E+05	9	828	17.05	1.4E+04	1.2E+05	1.7E+05
10	2,748	14.19	3.9E+04	2.8E+05	4.4E+05	10	1,265	18.11	2.3E+04	2.1E+05	2.7E+05
11	2,902	14.25	4.1E+04	2.9E+05	4.7E+05	11	2,724	16.83	4.6E+04	3.9E+05	5.7E+05
12	1,582	14.93	2.4E+04	1.8E+05	2.6E+05	12	2,847	17.11	4.9E+04	4.2E+05	6.0E+05
13	3,978	15.91	6.3E+04	5.0E+05	6.4E+05	13	3,318	17.13	5.7E+04	4.9E+05	7.0E+05
14	3,075	13.81	4.2E+04	2.9E+05	5.0E+05	14	863	17.21	1.5E+04	1.3E+05	1.8E+05
15	3,132	13.89	4.4E+04	3.0E+05	5.1E+05	15	4,533	18.10	8.2E+04	7.4E+05	9.6E+05
16	11,480	14.00	1.6E+05	1.1E+06	1.9E+06	16	1,483	16.41	2.4E+04	2.0E+05	3.1E+05
17	3,092	14.26	4.4E+04	3.1E+05	5.0E+05	17	1,375	17.48	2.4E+04	2.1E+05	2.9E+05
18	3,802	13.30	5.1E+04	3.4E+05	6.2E+05	18	2,151	17.98	3.9E+04	3.5E+05	4.5E+05
19	2,177	13.94	3.0E+04	2.1E+05	3.5E+05	19	1,274	16.80	2.1E+04	1.8E+05	2.7E+05
20	699	14.94	1.0E+04	7.8E+04	1.1E+05	20	4,075	16.36	6.7E+04	5.5E+05	8.6E+05
21	1,021	14.69	1.5E+04	1.1E+05	1.7E+05	21	1,616	17.10	2.8E+04	2.4E+05	3.4E+05
						22	2,209	17.68	3.9E+04	3.5E+05	4.7E+05
						23	12,968	17.48	2.3E+05	2.0E+06	2.7E+06
						24	7,625	17.02	1.3E+05	1.1E+06	1.6E+06
						25	4,192	16.96	7.1E+04	6.0E+05	8.8E+05
						26	6,089	16.64	1.0E+05	8.4E+05	1.3E+06
						27	2,419	17.45	4.2E+04	3.7E+05	5.1E+05
						28	3,099	17.04	5.3E+04	4.5E+05	6.5E+05

Note. m is mass, v is impact velocity, P is the total momentum upon ground impact, E_k is impact kinetic energy, and E_p is potential energy.

in $V_{\text{frag}} > 0.05$). The latter was finally selected to define whether F had occurred, based on the fact that trifling block chips would come off from many blocks after impacts. The differences are illustrated in Table A2.

2.2.4. Impact Velocity

Three videos were recorded for each block release, using the deployed HSVCs. By combining the videos, these data were used to determine velocities as follows: First, the terrain coordinates of the GCPs were obtained from topographic measurements, to centimeter accuracy. This provided a spatial reference framework and so added to the temporal framework provided by the HSVCs. When both frameworks are combined, positions, velocities, and accelerations can be calculated. Second, the terrain coordinates of each block were obtained by applying photogrammetry to the previously synchronized frames. Initially, this part of the process requires the image coordinates of the GCPs measured from each frame to be associated with their corresponding terrain coordinates, by means of the central projection equations. Once enough points with an appropriate distribution have been ascribed image and terrain coordinates, the position of the projection center and the camera orientation can be calculated. The technique is called external orientation (Hartley & Zisserman, 2003). Once the external orientation of the three cameras has been performed, the terrain coordinates of any point visible in at least two cameras (e.g., points on the surface of a block) can be computed by measuring the image coordinates from the frames. For this case, the terrain coordinates of the blocks were calculated roughly every 0.1 s and so were the velocities. The positioning mean square error was estimated to be about ± 0.05 m; thus, the impact velocities that were obtained are very accurate. The procedure is explained in more detail in Prades et al. (2017).

2.2.5. Potential Energies and Kinetic Parameters

Potential energies and the following kinetic parameters, whose relations to E_s values are explored in the results (section 3.1) are computed as follows: (i) potential energy ($E_p = mgh$), (ii) impact kinetic energy ($E_k = \frac{1}{2}mv^2$), (iii) momentum ($P = mv$), and (iv) mass ($m = \rho V_{3D}$); g is for gravity acceleration on the Earth's surface, h is height, and v is velocity. Here the total computed velocity ($v = \sqrt{v_x^2 + v_y^2 + v_z^2}$) is used, as obtained just before the main impact of each block on the quarry floor. The values are provided in Table 1.

3. Results and Discussion

3.1. Seismic Energy and Rockfall Kinetics

The application of equation (1) yielded values for seismic energy E_s between 0.3 and 35 J at Foj and 0.05 and 12 J at Ponderosa, for our BE of parameters. Figure 6 also depicts the range of values as obtained from 1,000 realizations picking a random value within the defined ranges for Q, c_R, and ρ for the rock substrate (see section 2.1.1). In terms of absolute values, impacts releasing higher seismic energy also varied more widely for the defined parameter range. Our BE was found to be between the 75th and 95th percentiles for most of the blocks, although it could be slightly higher in some specific cases (Figures 6c and 6d). The calculated E_{sT}/E_p ratios ($R_{s/p}$) were between 10^{-6} and 10^{-5} at Foj, whereas Ponderosa's blocks had values in between 10^{-7} and 10^{-5} (BE). The mean value obtained by considering all blocks was $1.40 \cdot 10^{-5}$ and $4.29 \cdot 10^{-6}$, respectively. E_s/E_k ratios ($R_{s/k}$) were mostly of the same order of magnitude for both quarries' blocks, with average values being $2.05 \cdot 10^{-5}$ (Foj) and $3.40 \cdot 10^{-6}$ (Ponderosa; Figure 7). The values may be systematically lower at Ponderosa due to a scree cone that formed on the quarry floor after subsequent releases, thus incrementing energy absorption by ground deformation. A mean seismic noise energy calculation before the impacts and within the 5- to 120-Hz passband was performed for each quarry following equation (1). The values of mean noise energy (scaled to impact waveform duration) that were obtained were always less than 0.1% of the seismic energy value without their removal (both quarries). Hence, we conclude that the seismic energy and energy ratios were not affected by noise within the frequency passband.

However, because of uncertainty in the parameters defining the ground properties, an estimate of the real accuracy of our BE result is difficult to provide here. Interestingly, while the considered likely variation in the aforementioned parameters may be great (see section 2.1.1), E_s values ranging from 5th to 95th percentiles were mostly in the same order of magnitude; the observation is similar when the full range is included (Figures 6c and 6d). Consequently, while the reported E_s result is subject to some level of uncertainty, the order of magnitude of the ratios with both E_p ($R_{s/p}$) and E_k ($R_{s/k}$) is reliable. While the conversion factor from E_p to radiated elastic energy in rockfalls seems to vary in the literature, it is usually low. For larger volumes (10^3 to 10^6 m^3), Deparis et al. (2008) found ratios between 10^{-6} and 10^{-3}. For smaller volumes (1 to 10^4 m^3), Hibert et al. (2011) obtained ratios in the range $10^{-5} - 10^{-3}$ by fitting simulated potential energy data to seismic energies retrieved from seismograms. This last result is in accordance with findings in Bottelin et al. (2014), who obtained ratios of 10^{-4} for two rockfalls of about $2 \cdot 10^3$ m^3. The variability in ratios within the same experiment has usually been attributed to the influence of nonlinear effects (the geotechnical characteristics of sites). Disparity is also found in studies focused on smaller rock volumes and seismic instrumentation located a few meters from impacts: Vilajosana et al. (2008) obtained a ratio as high as 0.25 for a 70-m^3 occurrence in the Montserrat massif, Catalonia. Conversely, Hibert, Malet, et al. (2017) propose a linear correlation between E_k and E_s for their data set from the French Alps, which yields ratios in the order of 10^{-6} for their E_k range (the authors compare E_s to the impacting kinetic energy, which is a fraction of the E_p). The type of rockfall could also have a strong influence on the result (e.g., Hibert et al., 2011). This would partially explain why the relative E_s obtained by Vilajosana et al. (2008) is much higher; they studied an event with a free fall of about 100 m, which contrasts with the controlled releases of blocks in a gully with gentle slope angles (~20° to 45°) by Hibert, Malet, et al. (2017). The tests performed here could be classified somewhere in the middle, being closer to those in Hibert, Malet, et al. (2017), as were the relative obtained E_s values ($R_{s/p}$ and $R_{s/k}$ in between 10^{-7} and 10^{-4}; see Figure 7).

No indication of the energy budget used in block breakage could be obtained for the tested blocks (i.e., no observable differences in radiated elastic energies between F and NF blocks). No particular impact geometry (IG) seems to systematically be the reason behind the low or high values either (Figure 7). Small relative E_s should be expected for impacts conducted herein mainly because of partial elasticity on ground contact (the block does not stop but bounces away). In addition, ground deformation and other dissipation effects (fragmentation, heat, or acoustic emission) could also explain the low efficiency that seems to dominate
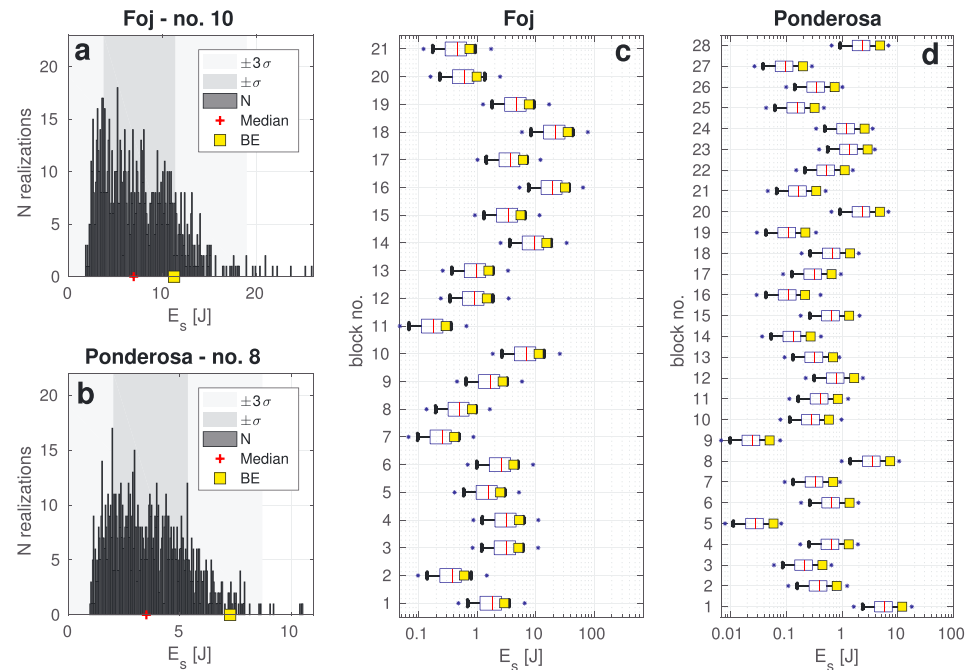
Figure 6. Seismic energy (E_s) result after 1,000 realizations varying Q, c_R, and ρ for the ground surface (see section 2.1.1). (a, b) Both histograms (Foj, Block 10, and Ponderosa, Block 8) represent a randomly selected example for each quarry displaying the result for a particular block and according to the legend. (c, d) Box plots indicating the median (red line), 25th and 75th percentiles (blue box), 5th and 95th percentiles (black whiskers), and full range (small blue stars) of the randomized calculation for each block at Foj and Ponderosa, respectively. Our best estimate (BE) is depicted with a yellow square.

the transference of both potential and kinetic to seismic energy (e.g., Vilajosana et al., 2008). This finding should be useful for further studies on the impacts (with or without fragmentation) of rockfalls on inclined slopes, as energy loss due to elastic radiation from the source could arguably be neglected. Differences obtained in the computed ratios (Figure 7) could be attributed to the following: (i) specific propagation characteristics (bouncing, rolling, and sliding of the blocks, which may influence the impact velocity, among other factors), (ii) block strength and damage (e.g., rock matrix strength, joint spacing, and persistence), (iii) local heterogeneities of the impact points and travel paths; the mineral exploitation at both quarries would likely have resulted in a shallow layer of infill material with different properties and thickness, over a surface of irregularly excavated rock, and (iv) damping factor α (see equations (1) and (4)) that is too simple to describe radiated elastic energy drainage in a fairly fractured and damaged medium. Bearing in mind the notable attenuation of high-frequency waves with distance, using multiple seismic recording devices at different distances would allow future studies to empirically determine energy attenuation as a function of frequency and r.

Definitive statements about the dominant factors (if any) and/or how they combine to influence this high variability in the computed E_s values and particularly in ratios cannot be provided without quantification, so is beyond the possibilities of this analysis. However, the scatter could arguably be attributed to ground heterogeneity as the main cause: as explained above, the main block impacts took place on a flat floor whose lithology is constant and equal to that of the blocks but filled with a thin layer of rock debris of irregular thickness, and likely to be fractured to some extent. In this setting, the tests were carried out under controlled conditions; all block falls were conveniently recorded with the equipment deployed in place, which allowed for high accuracy in the calculation of all kinetic measurements (see section 2.2). The range of impact velocities and block sizes was similar (see Tables 1 and A1), and neither block strength (L-hammer measurements; section 2.2.3) nor impact geometry (plotted in Figure 7 onward) could explain the variability. We acknowledge that the blocks' internal structure is subject to some degree of uncertainty; nevertheless, it is precisely by elimination of the aforementioned directly related factors that we reason that the other element at play (the terrain) should account for the scatter (i.e., fill thickness, compaction, and local buried bedrock fractures).
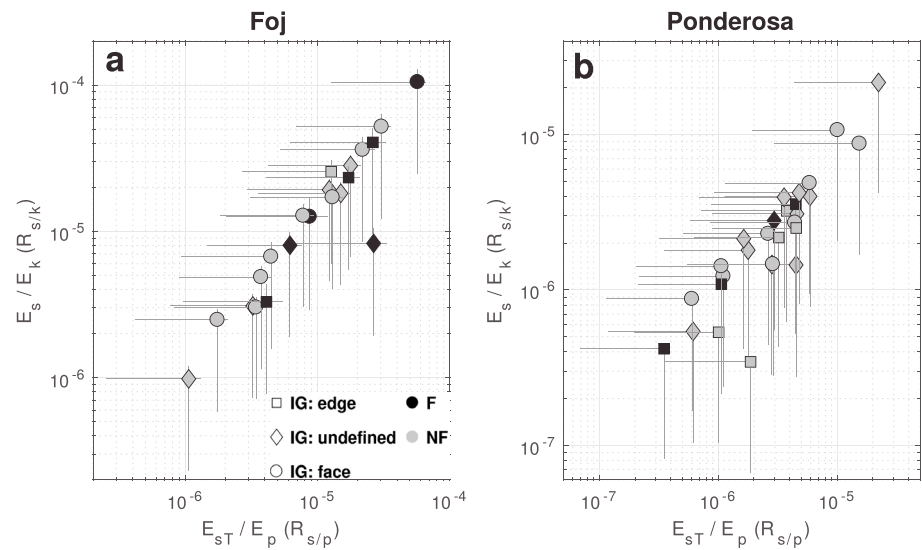
Figure 7. Ratios of seismic energy to potential (*X* axis) and kinetic (*Y* axis) energies, for Foj's (a) and Ponderosa's blocks (b). Horizontal and vertical bars in gray show the 5th and 95th percentiles of the randomized calculation for E_s (shown in Figure 6) and E_{sT}. The marker's edge type corresponds to impact geometry (IG) as determined from the video analysis for each of the released blocks; undefined is indicated when IG could not be determined from the video analysis. Color differentiates F and NF blocks.

Next, we report the comparison of seismic energy values with kinetic parameters as shown in Figure 8. In addition to examining E_k and E_p (Figures 8a and 8g), we compared the seismic energies that were obtained with the following: (i) E_p (Figures 8b and 8h), (ii) E_k (Figures 8c and 8i), (iii) mass (*m*; Figures 8d and 8j), (iv) vertical momentum ($P_z = mv_z$; Figures 8e and 8k), and (v) momentum (*P*; Figures 8f and 8l). A log scale was used, as the data span various orders of magnitude. Markers are plotted for our BE, along with error bars corresponding to 5th–95th percentiles of the randomized calculation shown in Figure 6, which was described above. As expected for blocks that roll down the same slope, high correlation is displayed between E_p and E_k. However, the ratio of kinetic to potential energy can be as low as 0.5 for Foj's blocks and 0.6 for Ponderosa's, which means that the amount of energy lost along the inclined slope (before the main impact) can already reach 50% of the initial value (Figures 8a and 8g). Seismic energy seems to scale with parameters (i) to (v) in a similar way, roughly following a linear trend. Consequently, a best-fit linear regression model was computed for each panel and is shown with a solid blue line. The corresponding equations are provided in each legend. The determination coefficients R^2 were low, close to 0.3–0.5 at Foj and around 0.2–0.4 at Ponderosa. However, p_{values} were between 10^{-4} and 0.015 and so should provide support for discarding the null hypothesis that there is no linear correlation between the plotted variables. Thus, while the correlation should be significant, our results suffer from high dispersion. The highest correlation was obtained for E_s versus P_z at Foj (panel e; R^2 of 0.47). The theoretical approach by Farin et al. (2015) reports that a scaled vertical momentum parameter ($mv_z^{13/5}$) should correlate with E_s, but this was tested here and did not significantly improve the previous determination coefficients (the obtained R^2 at Foj was 0.50, marginally above 0.47). The determination coefficients were slightly lower after testing $mv_z^{0.5}$, which had previously been found to provide the best correlation by Farin et al. (2015) and had also been recently employed by Hibert, Malet, et al. (2017), who obtained $R^2 \sim 0.5$.

Disparity in our results could be attributed to factors (i) to (iv) stated above with regard to the E_s values. Farin et al. (2015) also explain how sampling rates that are too low for the fully generated spectrum to be recovered may prevent the determination of a true total value of E_s. They use this argument to justify that seismic energies as obtained from rockfalls in their study do not appear to follow a theoretically derived scaling with $mv_z^{13/5}$. However, this could hardly be the reason behind the weak correlations found in our study; signals were recorded with a sampling frequency of 250 Hz (frequencies up to 125 Hz are visible), which covers all observable energetic frequencies reaching the recording distance, as shown in the spectrograms (Figures 3 and 4). Additionally, this comment is supported by a brief analysis of the theoretical frequency peaks predicted at the impact point, as noted above in section 2.1.1 and detailed in Appendix C. For most cases, the energy of the theoretical spectral velocity peaks above the Nyquist frequency only represents, a 2.4% or less
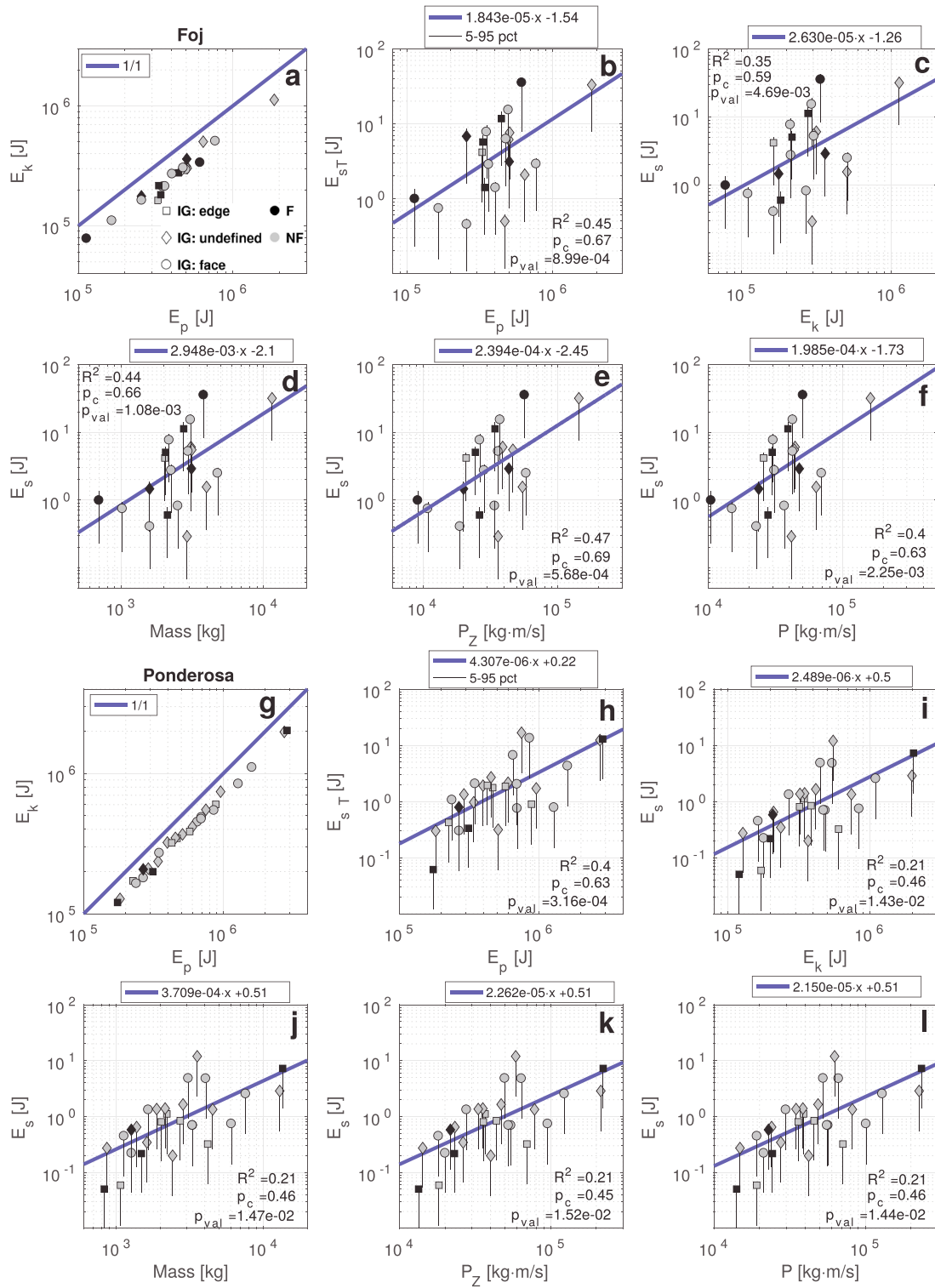
Figure 8. Seismic energy result and comparison with kinetic parameters and potential energies. Parameter abbreviations are in accordance with nomenclature defined and used in the text. Except for panels (a) and (g), which show a 1 to 1 line, the trend lines are best-fit linear regression models and the equations are shown in the corresponding legends. The plots also provide the coefficient of determination (R^2), coefficient of correlation (p_c), and p_{values}. Black lines extending from the markers refer to the 5th to 95th percentiles of the randomized calculation shown in Figure 6. The marker's edge type corresponds to impact geometry (IG), as determined from the video analysis for each of the released blocks; undefined is indicated when IG could not be determined from the video analysis. Color differentiates F and NF blocks.

of the energy in the frequency band that we capture and so supports rejection of the hypothesis that we cannot account for energetic frequencies higher than our Nyquist frequency, set at 125 Hz. In accordance with Hibert, Malet, et al. (2017), we suggest that mass and velocity might be controlling the generation of seismic signals in a similar way, or perhaps one of the two is of paramount importance. The results in Figure 8 do not allow us to infer which physical parameter(s) are conclusively the driving factor behind the recorded seismic signals.

Marker edges in Figure 8 also provide the IG of ground impacts, but there were no systematic differences in terms of E_s between blocks impacting face first and those edge first. An additional observation regarding fragmentation and impact geometry is that only 2 out of 10 blocks impacting face-first broke at Foj, and none at Ponderosa; moreover, three out of the four blocks impacting edge first broke at Foj, but the percentage was lower at Ponderosa (three out of eight; see Table A2). Other parameters that were tested for possible scaling with E_s were the impact velocity and impacting angle (measured from the horizontal); no scaling was found.

3.2. Rockfall Volumes Inferred From Seismic Energy

In this section we follow the approach proposed by Hibert et al. (2011), who showed that the seismic and potential energies of rockfalls were linked (Hibert et al., 2011, 2014). They obtained an analytical solution that yields the potential energy lost by a granular flow propagating down a flat slope. This expression is a function of the detached mass volume; then, provided the ratio of seismic to potential energy for a source area is known, it may be used to calculate the rockfall volume based on recovered seismic energy values (equation (10)). We consider the quarry floor where blocks stop their motion at height $h = 0$; thus, $|\Delta E_p| = E_p$ (initial).

$$V_{Ep} = \frac{3E_s}{R_{s/p}\rho gL(\tan\delta \cos\theta - \sin\theta)} = \frac{3E_p}{\rho gL(\tan\delta \cos\theta - \sin\theta)}, \qquad (10)$$

where ρ is directly the block density, considering that the fraction of solid material is 1 for an individual block (i.e., the volume of the propagating mass equals the volume of the block itself), g is the gravitational acceleration, L is the slope length ($\approx$20 m at Foj and $\approx$ 25 m at Ponderosa), θ is the mean angle of the slope ($\approx$60° at Foj and $\approx$70° at Ponderosa), and δ is the average angle between the deposit surface and the slope face (see Figure 1). The blocks stopped their motion on the flat floor; hence, we take $\delta = 180 - \theta$ for our particular case (i.e., the block *is* the deposit once its motion becomes 0 and is parallel to the flat floor). As block size was accurately determined by means of 3-D models of each block, this was a good opportunity to assess the result by applying equation (10) under the experimental conditions of the performed single-block rockfalls. As described above, loss of potential energy along the slope was significant ($E_k < E_p$); therefore, the estimation of volumes was also performed by employing the impacting kinetic energies (instead of the total potential energy) in equation (10).

Results are displayed in Figure 9, where it is shown that volumes determined with potential energies (V_{Ep}) are constantly 50% higher than the true volume V (as determined from the 3-D block models, V_{3D} in Table A1). This result is very similar to the validation case reported in Hibert et al. (2011), who obtained a computed volume approximately 1.43 times that of the detached mass (estimated by means of photogrammetry). Ratios V_{Ep}/V are constant because potential energies were determined using the block masses, which were themselves computed by means of the true volume and the rock block density; this results in the right-hand side of equation (10) being a constant $[C = f(\delta, \theta)]$ times the true volume. However, when kinetic energies are used, the volumes (V_{Ek}) that are obtained are much closer. They are not constant, because in this case impacting velocities v enter the equation. The mean of the ratios (V_{Ek}/V) is 0.94 for Foj's blocks (Figure 9a) and 1.07 for those tested at Ponderosa (Figure 9b), and the standard deviation is of 0.093 and 0.066, respectively. Another option in the calculation would have been to take the angle δ to be 0 (Hibert et al., 2011, 2014), considering that the slope angle is substantially larger than the friction angle of the rock and that blockfall propagation is stopped by the quarry floor (i.e., any deposit along the slope must be parallel to its inclination). This was tested and worsened the volume estimations reported above by an increase of roughly 50%. Moreover, because most of the released mass did not stop along the slope but on the quarry floor, we consider that the procedure that was used fit better in the context of our tests.
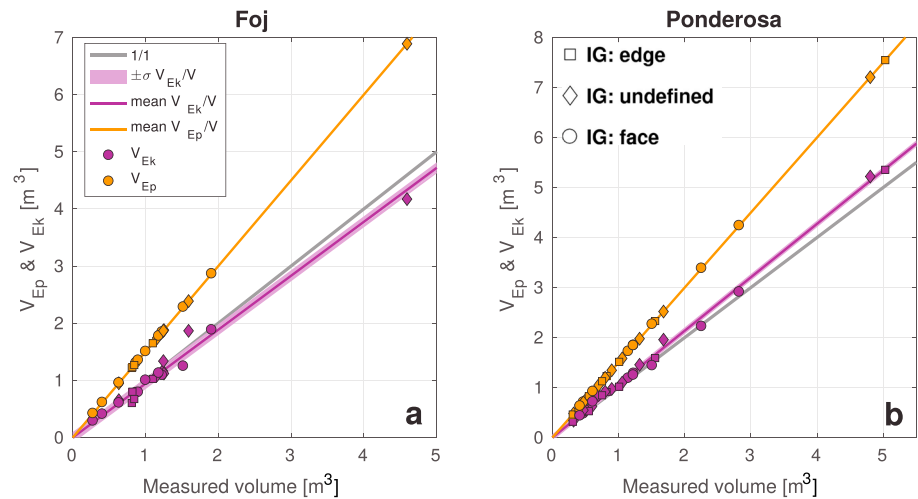
Figure 9. Computed values of V_{Ek} and V_{Ep} and their relation to measured volumes (V). (a) Foj blocks and (b) Ponderosa. The plots also show the mean value of the ratios between the calculated and true volumes and the standard deviation (σ) for V_{Ek}/V. The standard deviation of V_{Ep}/V is 0 (see text in section 3.2). In this plot, we do not distinguish between fragmented and nonfragmented blocks, and the marker's edge type corresponds to impact geometry (IG), as determined from the video analysis for each of the released blocks; undefined is indicated when IG could not be determined from the video analysis.

Our finding that V_{Ek} is closer to the real volume (Figure 9) is linked with total recovered seismic energies (E_{sT}) that mainly resulted from the impact on the horizontal quarry floor. This result is significant because impacting kinetic energy could be a more representative quantity than the total fall height energy, for the estimation of rock properties of rockfalls on slopes. Hence, further studies that explore this issue in more detail are needed, as is an analysis over a greater size span (the masses used in this analysis expand less than 2 orders of magnitude from 699 to 13,581 kg). Of course, the usage of impacting kinetic energies in real cases might be less convenient, as it would demand previous knowledge of energy loss during the fall path before the main impact. Furthermore, it is worth recalling that variation in the computed E_s values and ratios was found to be substantial for very similar rockfalls at each quarry. Although other unknown factors could be at play, ground heterogeneity seems likely to be the main factor causing this scatter (see the discussion in section 3.1 above). Hence, considering that the quarry setting where seismic signals propagated was probably more homogeneous than most natural sites, we must conclude that accurately estimating rockfall volumes just by employing E_s does not seem feasible at this point (i.e., when neither E_p or E_k are known).

3.3. Fragmentation on Seismic Recordings as Expressed in the Frequency and Time Domains

Results of the frequency analysis of block impacts on the quarry floor are shown in Figure 10. In summary, the plots show that blocks that fragmented on ground impact (red lines and black markers) are repeatedly linked with higher-frequency seismic signals (i.e., most energy is released at higher frequencies); this confirms what was first seen in spectrograms after processing the data (Figures 3 and 4). The mean spectra show that non-fragmented (NF) blocks release most of their energy at lower frequencies than fragmented (F) blocks, and vice versa (Figures 10a and 10d). For Foj's blocks, the spectral centroid (f_{CTR}) manages to separate both populations (fragmented, F, and nonfragmented, NF) better than the predominant frequency (Figures 10b and 10e). The same is observed for Ponderosa's blocks; even if the set of F samples for this quarry comprises just four blocks, the NF blocks' mean (which counts with 24 blocks) is revealed to be distinctly lower. Values (in Hz) are 56.62 ± 2.88 and 48.46 ± 4.39 at Foj and 52.84 ± 12.73 and 38.14 ± 4.73 at Ponderosa. Dominant frequencies obtained for the accelerograms corresponding to Foj's NF blocks are higher than the analogous values for Ponderosa quarry. In addition, F blocks seem to have less variability when it comes to BW (Figures 10c and 10f).

A time analysis is provided in Figure 11. The stacks (mean) of the signal envelopes manage to capture some existing differences in the time domain. From an observation of Figures 11a and 11f, it can be said that while the maximum acceleration is achieved at the beginning of the signal for both F and NF groups, F signals decay
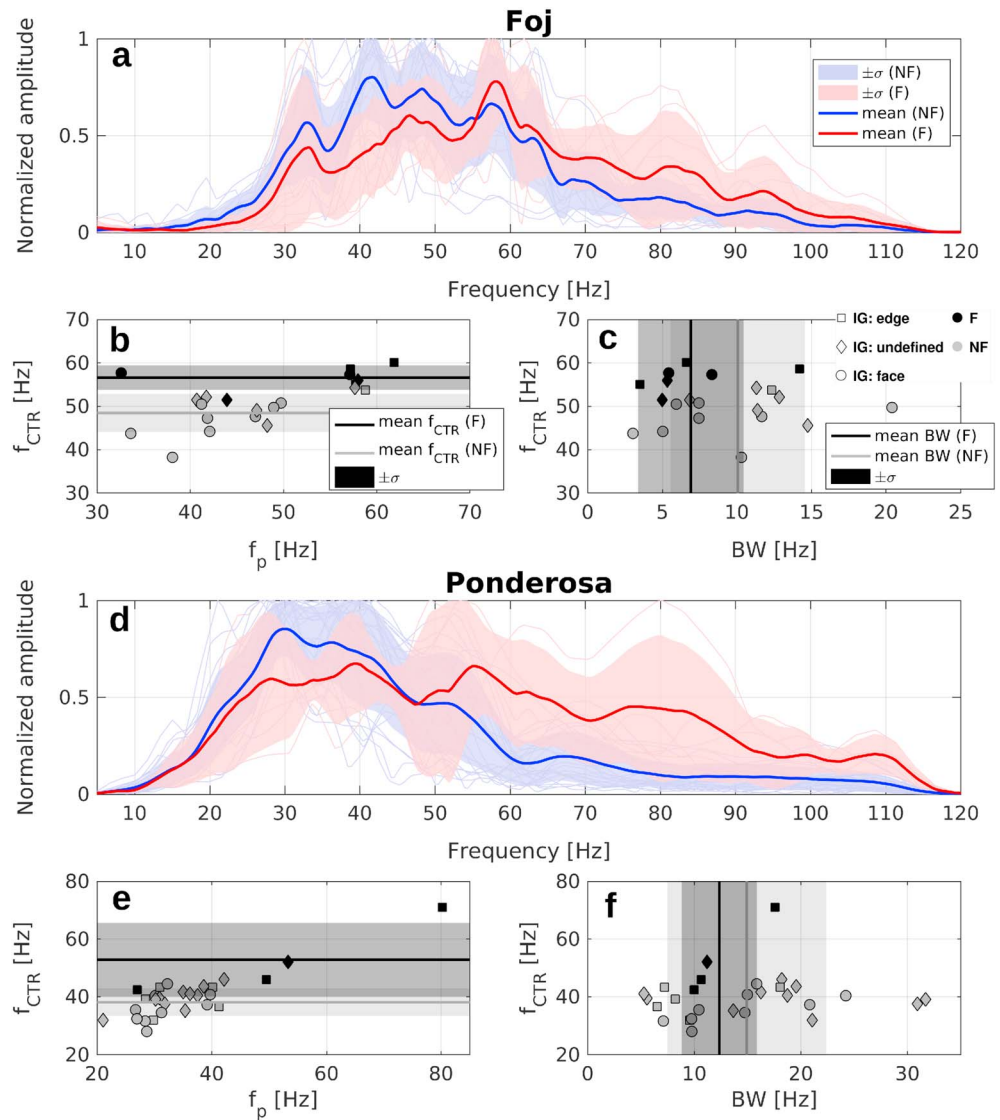
Figure 10. Analysis of fragmentation in the frequency domain. (a, d) A stack (mean) of all acceleration spectra and their standard deviation ($\pm\sigma$), superposed on all spectra. Means and standard deviations are computed at each plotted frequency sample. Spectra are normalized with respect to their maximum amplitude value. NF data are blue, and F are red. (b, c, e, and f) The predominant frequency, f_p, the frequency centroid, f_{CTR}, and bandwidth, bandwidth (BW; see section 2.1.2 for definitions). Means and standard deviations are provided for f_{CTR} and BW. The marker's edge type corresponds to impact geometry (IG), as determined from the video analysis for each of the released blocks; undefined is indicated when IG could not be determined from the video analysis. Color differentiates F and NF blocks.

somewhat slower in time than NF signals. However, the differences are subtle at Foj, where more F data are available. The reported parameters allow each signal's duration (BD and ID), intensity (I_A), and impulsiveness (R_{pem}) to be characterized, according to the methodology employed (section 2.1.2). The BD of the ground impacts themselves oscillate between 0.1 and 0.5 s for most cases and are slightly greater for Foj impacts (Figures 11b and 11g). The ID ratio is less than 1 for all signals but one at each quarry (Figures 11c and 11h). This was an expected result because the energy that an impactor transmits to the ground should be maximum near the beginning (initial time) and then diminish. Neither I_A nor R_{pem} manage to capture differences between F and NF blocks; thus, none of the individual parameters succeeded in characterizing fragmentation (Figures 11b–11e and 11g–11j).

Spectral analysis of seismic signals showed higher dominant frequencies than those appearing in seismic recordings resulting from natural rockfalls (e.g., Dammeier et al., 2011; De Santis et al., 2016; Hibert et al., 2011). This result could be explained by the greater density of quarry bedrock in comparison to previous studies'
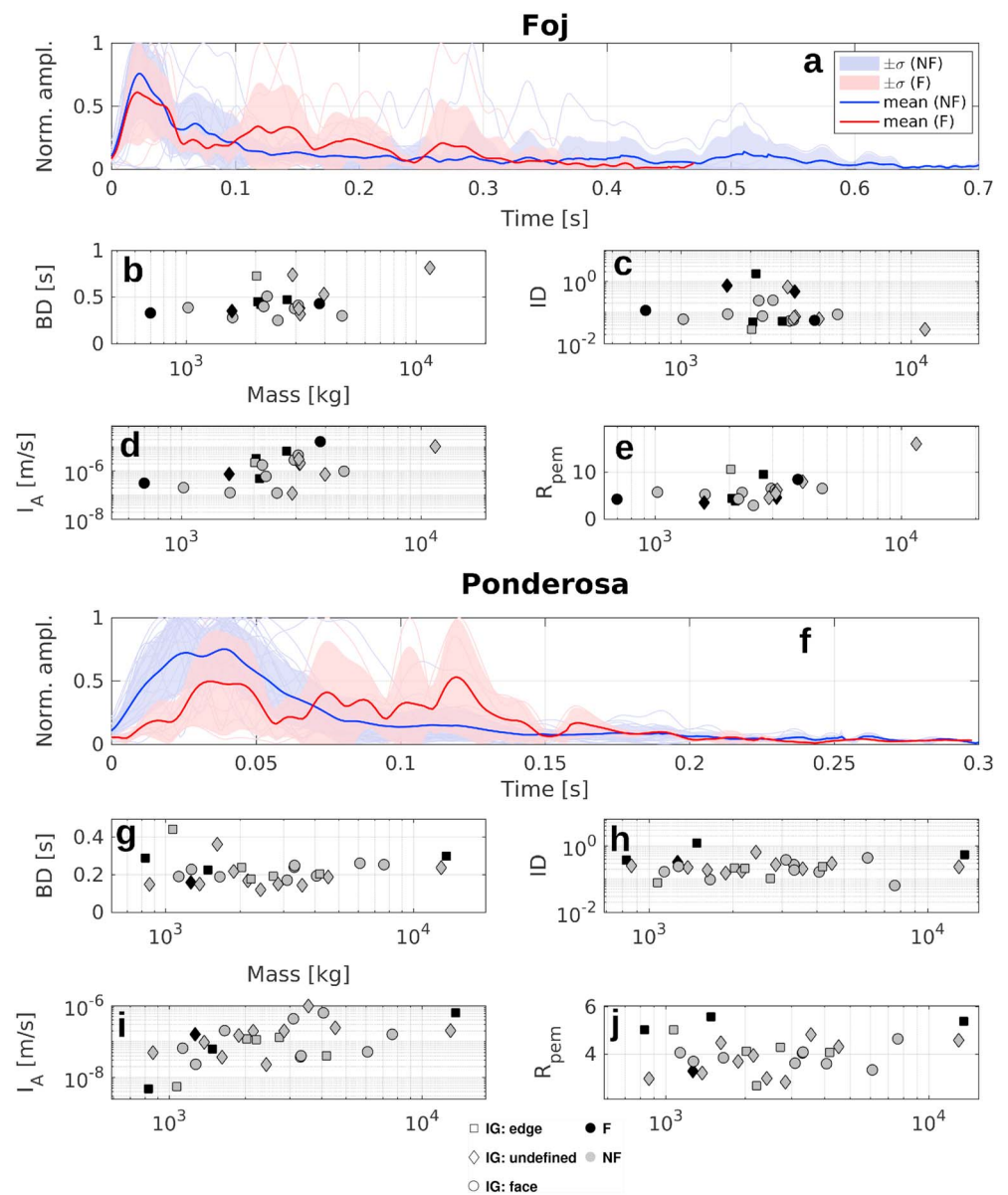
Figure 11. Analysis of fragmentation in the time domain. (a, f) A stack (mean) of all envelopes (computed as in equation (3) for the maximum component; here envelopes are also normalized to the maximum value of each event), and their standard deviation reach ($\pm\sigma$), superposed on all envelopes. Means and standard deviations are computed for each plotted time sample. NF data are blue, and F are red. Parameters shown in (b)–(e) and (g)–(j) are the bounded duration (BD), increasing/decreasing time ratio (ID), arias intensity (I_A), and ratio of the envelope peak to the envelope mean (R_{pem}; see section 2.1.2 for definitions). Mass is displayed along the X axes of these plots. The marker's edge type corresponds to impact geometry (IG), as determined from the video analysis for each of the released blocks; undefined is indicated when IG could not be determined from the video analysis. Color differentiates F and NF blocks.

settings (e.g., granular terrace in Vilajosana et al., 2008, volcanic rocks in Farin et al., 2015; Hibert et al., 2011, 2014, or marls in Hibert, Malet, et al., 2017) and the short distance source (impact) to signal, which may be driving the observed frequencies more than the initial impact (e.g., Tsai et al., 2012). While signal attenuation was accounted for in the calculation of seismic energies (α coefficient; section 2.1.1), it is neglected for this part (section 3.3) because the focus is on the relative variation between F and NF impacts. Block breakage was essentially characterized by higher energetic frequencies (relative to those of NF blocks; see Figures 10a, 10b, 10d, and 10e). Acknowledging the variability obtained in the energy ratios (section 3.1), observed differences between F and NF spectra/signals could partially respond to distinct block propagation, damage, and impact ground heterogeneities (i.e., seismic signals of F blocks dominated by higher frequencies because

of a stiffer impact ground). However, our findings with nearly no frequency overlap between F and NF blocks seem to capture the intrinsic breakage phenomena (fracture growth) and are supported by statistically significant correlations between fragmentation/number of fragments (see Table A2) and f_{CTR}: p_{values} are of 3E−04 and 1E-03 at Foj, and 2E−04 for both fragmentation and number of fragments at Ponderosa. Therefore, our results agree with those from previous studies investigating precursory signals of mass detachment in rock-fall processes, which had already linked short-period seismic signals with crack propagation phenomena (e.g., Arosio et al., 2015; Helmstetter & Garambois, 2010; Levy et al., 2011). As regards the time domain, the observed slower amplitude decay of F signals could be linked to the block fragmentation process as well. Unfortunately, because we cannot quantify the effect of the interplay among block/terrain properties nor the presence of damage in the impacting ground, further comments are outside the scope of the paper.

4. Conclusions

This paper presents the analysis of accelerometric recordings associated with two sets of real-scale single-block experimental rockfalls. Seismic energies (E_s) have been studied in absolute and relative terms (to that of the potential (E_p) and main impact kinetic (E_k) energies) and for possible scaling with kinetic parameters (section 3.1). Volumes of blocks have been inferred by employing E_s and their relation to both E_p and E_k (section 3.2). Finally, the signature of fragmentation in the frequency and time domains has been explored (section 3.3). The most relevant findings of the study are as follows:

1. The computed ratios of seismic to both E_p and E_k energies spanned between 10^{-7} and 10^{-4} (Figure 7). For rockfalls on inclined slopes, this finding suggests that the fraction of impacting energy transmitted as seismic waves is not relevant.
2. While a statistically significant positive correlation was found between kinetic parameters and seismic energies, numeric fitting provided low determination coefficients (0.21 – 0.47; Figure 8). Both mass and impact velocity are known to play a role in the generation of seismic signals, but further studies are required to define whether there may be a unique dominant factor.
3. The best volume estimations were obtained by using the impact kinetic energy (Figure 9). Recorded seismic signals were seen to be dominated by the main impact; thus, the employment of seismic energy relative to E_k might be preferred for estimating rock properties of rockfalls on slopes, from the seismic signals they generate. However, given the observed variability in the computed ratios, it seems difficult to properly determine the volume of the falling mass without knowing E_p nor E_k.
4. Block breakage seismic signals were characterized by higher energetic frequencies (spectral centroid frequency of 56.62 ± 2.88 Hz at Foj and 52.84 ± 12.73 Hz at Ponderosa) when compared to those of nonfragmentation impacts (48.46 ± 4.39 Hz at Foj and 38.14 ± 4.73 Hz at Ponderosa); the spectral centroid managed to capture the differences as a single parameter (Figure 10). Fragmentation signals also displayed a slightly slower decay in the time domain (Figures 11a and 11f). Three out of four blocks impacting edge first at Foj fragmented, while only 2 out of 10 impacting face first did. At Ponderosa, none of the blocks impacting face first fragmented.
5. To diminish uncertainty when using seismic signals to retrieve rockfall characteristics, the usage of multiple seismic recording devices at various distances and covering the gap around the source point is recommended, as is the computation of a local attenuation model.

Appendix A: Additional Tables

This appendix provides additional information for the single-block rockfall experiments studied in this paper. For each block, Table A1 includes volumes and masses, and Table A2 shows the ground impact characteristics.

Table A1
On-Field Measured Volumes (V_1), Better Constrained Volumes From 3-D Models of the Released Blocks (V_{3D}), and Masses (m) Obtained for Each Studied Block at Foj (Left) and Ponderosa (Right)

Foj				Ponderosa			
No.	V_1 (m³)	V_{3D} (m³)	m (kg)	No.	V_1 (m³)	V_{3D} (m³)	m (kg)
1	1.2	1.2	3,114	1	1.0	1.3	3,556
2	0.8	0.8	2,113	2	0.5	0.8	2,025
3	0.7	0.8	2,050	3	0.4	0.4	1,131
4	1.2	1.2	2,959	4	0.6	0.6	1,655

Table A1 (continued)

	Foj				Ponderosa		
No.	V_1 (m³)	V_{3D} (m³)	m (kg)	No.	V_1 (m³)	V_{3D} (m³)	m (kg)
5	1.9	1.9	4,774	5	0.3	0.4	1,069
6	1.2	0.8	2,027	6	0.8	0.7	1,884
7	0.6	0.6	1,592	7	1.4	1.2	3,308
8	1.1	1.0	2,508	8	5.8	5.0	13,581
9	0.8	0.9	2,253	9	0.4	0.3	828
10	1.4	1.1	2,748	10	0.6	0.5	1,265
11	1.4	1.2	2,902	11	1.2	1.0	2,724
12	0.7	0.6	1,582	12	1.1	1.1	2,847
13	1.4	1.6	3,978	13	1.0	1.2	3,318
14	1.0	1.2	3,075	14	0.2	0.3	863
15	1.2	1.3	3,132	15	1.8	1.7	4,533
16	4.8	4.6	11,480	16	0.5	0.5	1,483
17	1.2	1.2	3,092	17	0.5	0.5	1,375
18	1.9	1.5	3,802	18	0.8	0.8	2,151
19	1.0	0.9	2,177	19	0.4	0.5	1,274
20	0.3	0.3	699	20	1.3	1.5	4,075
21	0.3	0.4	1,021	21	0.4	0.6	1,616
				22	0.8	0.8	2,209
				23	4.8	4.8	12,968
				24	2.6	2.8	7,625
				25	1.7	1.6	4,192
				26	0.8	2.3	6,089
				27	0.7	0.9	2,419
				28	0.6	1.1	3,099

Note. ρ is 2,500(Foj) and 2,700(Ponderosa) kg/m³.

Table A2
Main Ground Impact Information for the Blocks Considered in the Analysis

	Foj					Ponderosa			
No.	F	N_{frag}	V_{frag}	IG	No.	F	N_{frag}	V_{frag}	IG
1	1	5	0.19	2	1	0	2	0.00	2
2	1	53	0.66	3	2	0	1	0.00	3
3	1	55	0.60	3	3	0	1	0.00	1
4	0	1	0.00	1	4	0	3	0.04	1
5	0	4	0.03	1	5	0	1	0.00	3
6	0	1	0.00	3	6	0	10	0.02	2
7	0	1	0.00	1	7	0	12	0.01	1
8	0	1	0.00	1	8	1	44	0.21	3
9	0	1	0.00	1	9	1	32	0.22	3
10	1	123	0.56	3	10	1	38	0.14	2
11	0	19	0.04	2	11	0	2	0.01	3
12	1	22	0.17	2	12	0	1	0.00	2
13	0	9	0.00	2	13	0	1	0.00	1
14	0	1	0.00	1	14	0	29	0.01	2
15	0	1	0.00	2	15	0	1	0.00	2
16	0	1	0.00	2	16	1	68	0.67	3
17	0	5	0.01	2	17	0	8	0.00	2
18	1	35	0.07	1	18	0	54	0.01	2
19	0	3	0.01	1	19	0	1	0.00	1
20	1	74	0.80	1	20	0	2	0.00	1

Table A2 (continued)

	Foj					Ponderosa			
No.	F	N_{frag}	V_{frag}	IG	No.	F	N_{frag}	V_{frag}	IG
21	0	1	0.00	1	21	0	1	0.00	2
					22	0	4	0.05	3
					23	0	3	0.00	2
					24	0	1	0.00	1
					25	0	3	0.00	3
					26	0	1	0.00	1
					27	0	1	0.00	2
					28	0	1	0.01	1

Note. Column fields are as follows: identification number (no.), fragmentation (F; 1 = affirmative), generated number of fragments (N_{frag}), fragmented fraction relative to impacting volume (V_{frag}), and IG = block impact geometry (1 is face impact, 3 is edge/vertex, and 2 is undefined, i.e., it could not be determined from video analysis).

Appendix B: Three-Component Polarization Analysis

Equation (1) in the main text is commonly used in studies computing seismic energies from rockfalls (e.g., Hibert et al., 2011, 2014; Levy et al., 2015). Among others, this equation entails the assumption of surface waves dominating the recorded waveform. Taking advantage of our three-component (3-C) recordings, we provide the results of a quantitative polarization analysis to test whether the aforementioned hypothesis is realistic in our context. We employ the complex polarization filter of Vidale (1986) and follow his text in this part. The process is explained below:

The analytic signal of each component is obtained as in equation (B1), where u_r, v_r, and w_r represent the radial, transverse, and vertical time series, respectively. i is $\sqrt{-1}$, and H_t is the Hilbert transform:

$$u(t) = u_r(t) + iH_t(u_r(t))$$
$$v(t) = v_r(t) + iH_t(v_r(t))$$ (B1)
$$w(t) = w_r(t) + iH_t(w_r(t)).$$

Then, the covariance matrix is as follows:

$$C(t) = \begin{bmatrix} uu^* & uv^* & uw^* \\ vu^* & vv^* & vw^* \\ wu^* & wv^* & ww^*, \end{bmatrix}$$ (B2)

where in equation (B2), j^* is the complex conjugation of j. The eigenvectors ($[x_i \, y_i \, z_i]$) and eigenvalues (λ_i) of the 3×3 $C(t)$ matrix can be computed for each sample as in equation (B3):

$$\begin{bmatrix} x_i \\ y_i \\ z_i \end{bmatrix} [C - \lambda_i I] = 0, \quad i = 1, 2, 3.$$ (B3)

The maximum polarization is in the direction of the eigenvector $V_m = [x_m \, y_m \, z_m]$ associated with the largest eigenvalue λ_m. We then find the rotation that results in the maximum length of the real component of V_m by maximizing X. The search is made over $\psi = 0 - 180$ in 1° increments:

$$X = \sqrt{(\Re(x_m t_\psi))^2 + (\Re(y_m t_\psi))^2 + (\Re(z_m t_\psi))^2}$$
$$t_\psi = \cos\psi + i\sin\psi$$ (B4)

In (B4), $\Re(j)$ is the real part of j. Hence, the vector V_m is rotated $\psi°$. Among others, this analysis allows us to obtain P_E and P_S, where the former is a measure of the elliptical component of polarization and P_S indicates
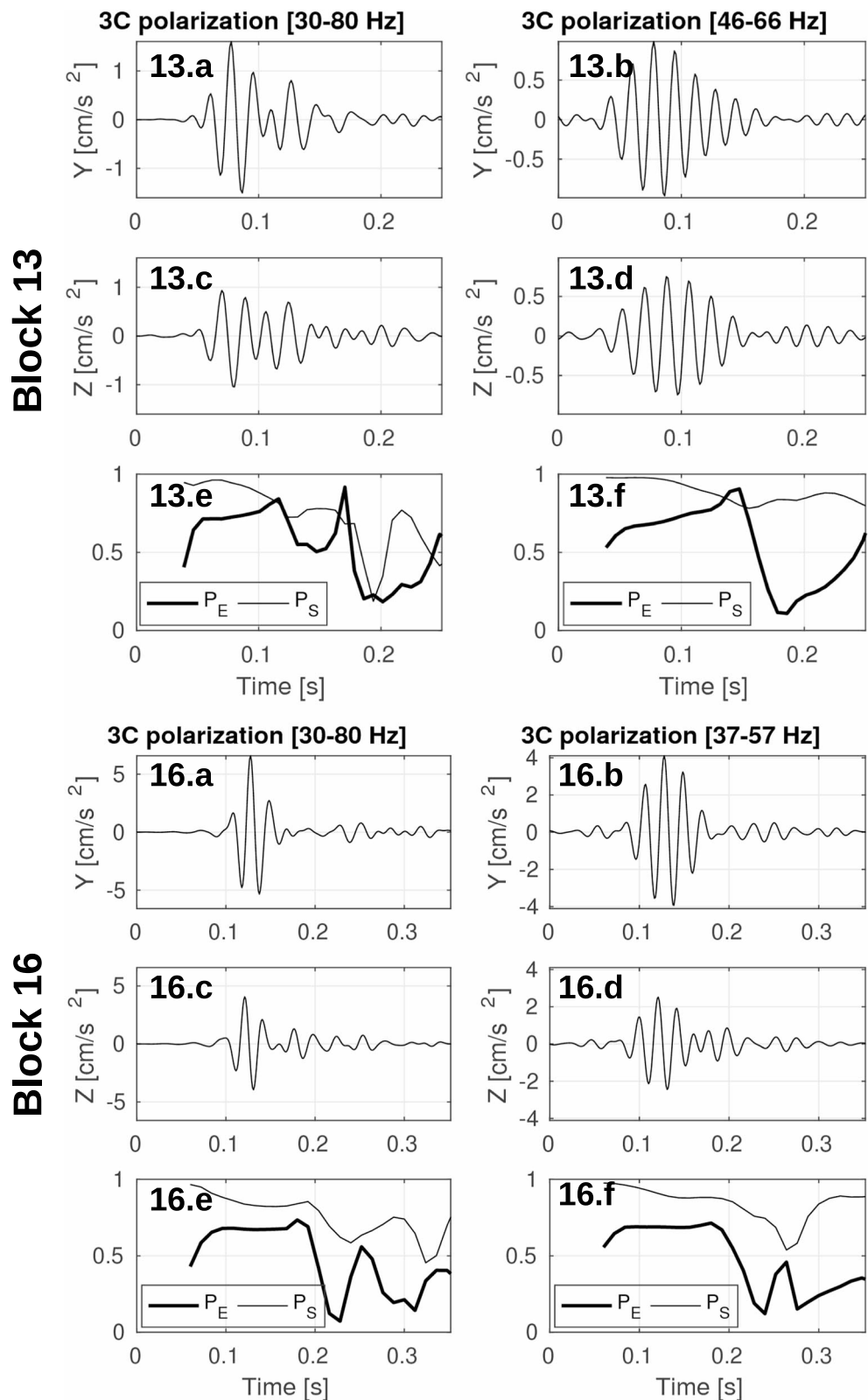
Figure B1. Results of the 3-C polarization analysis for two of the Foj blocks. (a, b) Accelerograms corresponding to the maximum component, in this case the radial. (c, d) Accelerograms corresponding to the vertical component. (e, f) Elliptical component of polarization (P_E) and strength of polarization (P_S), as obtained for the corresponding recordings. Each column shows signals and polarization results as obtained for the frequency passband indicated at the top. Note that the quantitative analysis employs the three components, even though the transverse is not plotted here.

the polarization strength (i.e., if there is a main component of polarization). Both parameters are between 0 and 1.

$$P_E = \frac{\sqrt{1-X^2}}{X}$$
$$P_S = 1 - \frac{\lambda_1 + \lambda_2}{\lambda_m},$$

(B5)

where λ_1 is the smallest eigenvalue and λ_2 is the intermediate. We compute P_E and P_S by means of a simple code that incorporates the procedure detailed in equations (B1)–(B5). The results are given for signals filtered with a third-order Butterworth filter between 30 and 80 Hz (wide passband) and for a narrower passband of f_{CTR} (equation (5)) ± 10 Hz, which restricts the analysis to the most energetic frequencies of each signal. After a trial and error process to provide stable estimations, we use a sliding window with length 0.1 times the number of samples, with 90% overlap, to estimate P_E and P_S over time. The analysis is performed for Foj signals because the radial and transverse components were already well aligned with two axes of the accelerometer.

The results display average values of $P_E \sim 0.5$ (entire impact signal) and maximum values during the strong phase of each waveform of 0.7–0.9. The strength of polarization P_S is high (~ 0.8 on average and maximum values >0.9). Results are very similar for both passbands, thus confirming that the waveforms with spectral content around the f_{CTR} dominate the signal. Graphic results are also provided in Figure B1 for two of the blocks. The wider passband (Figures B1a, B1c, and B1e) has minimum amplitude loss with respect to that used throughout the analysis (5–120 Hz; see section 2.1), though is somewhat more restricted to allow better visualization of surface waves in the accelerogram representation. From the figure it is clear that the strong phase of the waveform is dominated by elliptical polarization and that the strength of polarization is high (i.e., P_S values close to 1, thus estimations are reliable; see Vidale, 1986). In Figure B1, the expression of the observed waveforms is characteristic of Rayleigh waves as well. Therefore, this result supports the assumption of surface waves dominating the waveform, as implied by equation (1) in the main text.

Appendix C: Theoretical Frequency Peaks

In this section we follow the approach presented in McLaskey and Glaser (2010) to model a force pulse that simulates the impact of our blocks on the quarry floor. The goal is to obtain a broad picture of the expected spectral content for our impacts, at the point of impact. This methodology is used here to explore whether frequencies that are higher than our Nyquist frequency (the maximum observable frequency for a given sampling rate, in this case 125 Hz) have relevant amplitude peaks when compared to those that we can capture. Knowing that higher frequencies undergo increased attenuation with distance, this should help in understanding whether our seismic energy results would have been different by sampling at a higher rate and closer to the impact point. This analysis does not intend to be comprehensive but rather provide support for our comments stating that the scatter observed in our E_s results was unlikely to be due to a low sampling frequency (section 3.1 in the main text).

An impulsive force in the form of a "half-sine" can be used to simulate the impacts of a ball hitting a massive body (Hunter, 1957). Later, Reed (1985) corrected the equation derived by Hunter (1957) and proposed the following formulation (equation (C1)):

$$f(t) = f_{max} \sin(\pi t/t_c)^{3/2}, \quad 0 \le |t| \le t_c$$
$$f(t) = 0 \quad \text{otherwise.}$$

(C1)

In equation (C1), the time of contact (t_c) and maximum force (f_{max}) are expressed as follows:

$$t_c = 4.53(4\rho_1 \pi(\delta_1 + \delta_2)/3)^{2/5} R_1 v_0^{-1/5}$$

(C2)

$$f_{max} = 1.917\rho_1^{3/5}(\delta_1 + \delta_2)^{-2/5} R_1^2 v_0^{6/5},$$

(C3)

where in equations (C2) and (C3), R_1, v_0, and ρ_1 are the radius, impact velocity, and density of the ball, respectively. $\delta_i = (1 - v_i^2)/(\pi E_i)$, where E and v are the Young's modulus and Poisson coefficient and subscripts 1 and 2 refer to the ball and propagation medium materials, respectively. For our case, we consider the blocks as the ball and the quarry bedrock as the propagation terrain. We pick an approximate R_1 according to half
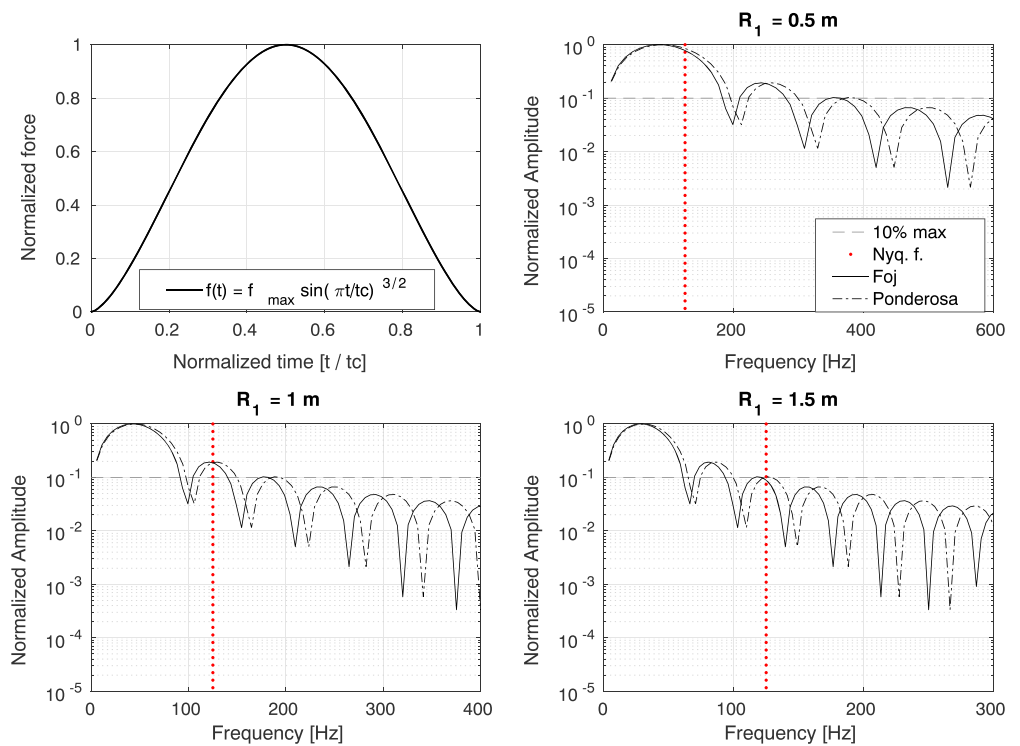
Figure C1. (a) Normalized plot of the simulated force pulse $f(t)$ and its equation (see text for parameter definitions). Note that, consistent with the rest of the text, normalizations are performed with respect to the maximum value of the variable displayed in the Y axis. In the case of (a), the time is also normalized as shown in the figure. (b–d) Spectrum of the $f(t)$ for three values of R_1, as obtained for the frequencies of interest. The plots show narrower frequency ranges for larger R_1 values because their amplitude decay increases. The gray discontinuous line serves as the 10% threshold of the maximum spectral velocity amplitude, and the red dotted line represents our Nyquist frequency (i.e., the maximum observable frequency, 125 Hz).

the largest diagonal of the block, v_0 is the average impact velocity for the studied blocks at each quarry (~14 m/s at Foj and 17 m/s at Ponderosa), and ρ_1 is 2,500 kg/m³ at Foj and 2,700 at Ponderosa. A v of 0.25 is taken for both the blocks and the horizontal quarry floor (propagation medium). E_1 (block) is 10 GPa at Foj and 30 GPa at Pondersa, whereas E_2 is 1 GPa for both quarries. The selected value of E_2 is smaller for the propagation terrain because both some superficial infill (due to standard exploitation works in the quarry) and mass waste (deposited after each block fall) were present in the impact terrain.

After generating the force pulse that simulates our impacts (equation (C1)), we obtain its expression in the frequency domain by using its integral definition (e.g., Brigham, 1973; Papoulis, 1962). This spectrum should scale with unattenuated displacements (refer to equations (1) or (2) in McLaskey & Glaser, 2010). Hence, to be consistent with our seismic energy computation, which uses the ground velocity envelope (refer to equation (1) in the main text), we convert it to spectral velocity by taking the product with the corresponding $i\omega = i2\pi f$ term. In this section, we avoid using a numerical FFT algorithm, in order to have better control of the spectrum resolution. The result is depicted in Figure C1, with Figure C1a showing the force pulse.

In Figures C1b–C1d, the maximum amplitude is always within our frequency range (up to 125 Hz). The smaller radius (Figure C1b) is used to represent the few cases where the volume is less than 0.5 m³ (refer to Table A2). For this scenario, the energy at frequencies higher than 125 Hz can still be important. However, for larger blocks, the energy that the Hertz impulse theory predicts at frequencies above 125 Hz is substantially lower. To provide additional quantitative evidence, the energy ratio between the theoretical spectral velocities ($V(\omega)$) of frequencies 5–120 Hz (the interval used when calculating E_s, refer to equation (1)) and those in the range 120–1,500 Hz was computed. The latter represent the energy, which would be "lost" due to network shortcomings. This does not imply that the impacts do not generate energy above 1.5 kHz; however, this upper limit was chosen as theoretical spectral velocity peaks above that frequency have, for the three R_1 cases explored, amplitudes that are below 1% of the maximum. Hence, they do not meaningfully contribute to the integral

when the energy is computed (equation (C4)). Note also that the upper frequency interval is already 12 times wider than the lower one. Here we define the energy spectral density ($| V(\omega) |^2$) to obtain the total energy (E) in a finite frequency interval, which is computed as follows:

$$E = \frac{1}{2\pi} \int_{f_1}^{f_2} | V(\omega) |^2 \, d\omega, \tag{C4}$$

where f_1 and f_2 are the lower and upper frequency for each interval. Hence, E in equation (C4) was calculated for each of the two frequency intervals. Then, the ratio of the lower-frequency interval over the higher-frequency interval was obtained. The ratios were found to be 5.72, 48.23, and 120.98 (Foj) and 3.43, 33.89, and 94.77 (Ponderosa), for the three considered values of R_1, that is, 0.5, 1, and 1.5 m. Averaging results, these ratios correspond to E losses of 17.94%, 2.4%, and 0.9%, respectively, under the working assumption that frequencies above 1.5 kHz are negligible. These results show that the determined absolute E_s values might fall slightly short of their true value, but the amount of energy that we do not capture is small enough that it would not interfere with the following: (i) the results for the tested scaling relationships (note that almost all blocks have $R_1 > 0.5$), let alone (ii) our claim that E_s is not relevant when compared to E_p and E_k (which are various orders of magnitude larger, see section 3.1).

References

Aki, K., & Richards, P. G. (1980). *Quantitative seismology: Theory and methods* (Vol. 1). Sausalito, CA: University Science Books.

Allstadt, K. (2013). Extracting source characteristics and dynamics of the August 2010 Mount Meager landslide from broadband seismograms. *Journal of Geophysical Research: Earth Surface*, *118*, 1472–1490. https://doi.org/10.1002/jgrf. 20110

Amitrano, D., Arattano, M., Chiarle, M., Mortara, G., Occhiena, C., Pirulli, M., & Scavia, C. (2010). Microseismic activity analysis for the study of the rupture mechanisms in unstable rock masses. *Natural Hazards and Earth System Sciences*, *10*(4), 831–841.

Arias, A. (1970). Measure of earthquake intensity. In R. J. Hansen (Ed.), *Seismic design for nuclear power plants* (pp. 438–483). Cambridge, US, University of Chile, Santiago de Chile: Massachusetts Institute of Technology Press.

Arosio, D., Longoni, L., Papini, M., & Zanzi, L. (2015). *Analysis of microseismic activity within unstable rock slopes in modern technologies for landslide monitoring*. Berlin, Heidelberg: Springer. https://doi.org/10.1007/978-3-662-45931-7

Assefa, S., McCann, C., & Sothcott, J. (2003). Velocities of compressional and shear waves in limestones. *Geophysical Prospecting*, *51*(1), 1–13.

Bommer, J. J., & Boore, D. M. (2004). Engineering Seismology.

Boore, D. M., & Thompson, E. M. (2014). Path durations for use in the stochastic-method simulation of ground motions,. *Bulletin of the Seismological Society of America*, *104*, 2541–2552. https://doi.org/10.1785/0120140058

Bottelin, P., Jongmans, D., Daudon, D., Mathy, A., Helmstetter, A., Bonilla-Sierra, V., et al. (2014). Seismic and mechanical studies of the artificially triggered rockfall at Mount Néron (French Alps, December 2011). *Natural Hazards and Earth System Sciences*, *14*(12), 3175–3193. https://doi.org/10.5194/nhess-14-3175-2014

Brigham, E. O. (1973). *The fast Fourier transform: An introduction to its theory and application* (pp. 252). Englewood Cliffs, NJ: Prentice Hall.

Chen, C.-H., Chao, W.-A., Wu, Y.-M., Zhao, L., Chen, Y.-G., Ho, W.-Y., et al. (2013). A seismological study of landquakes using a real-time broad-band seismic network. *Geophysical Journal International*, *194*(2), 885–898.

Corominas, J., Lantada, N., Gili, J., Ruiz-Carulla, R., Matas, G., Mavrouli, O., et al. (2017). The RockRisk project: Rockfall risk quantification and prevention. In *6Th Interdisciplinary Workshop on Rockfall Protection Rocexs 2017*.

Dahlen, F. (1993). Single-force representation of shallow landslide sources. *Bulletin of the Seismological Society of America*, *83*(1), 130–143.

Dammeier, F., Moore, J. R., Hammer, C., Haslinger, F., & Loew, S. (2016). Automatic detection of alpine rockslides in continuous seismic data using hidden Markov models. *Journal of Geophysical Research: Earth Surface*, *121*, 351–371. https://doi.org/10.1002/2015JF003647

Dammeier, F., Moore, J. R., Haslinger, F., & Loew, S. (2011). Characterization of alpine rockslides using statistical analysis of seismic signals. *Journal of Geophysical Research*, *116*, F04024. https://doi.org/10.1029/2011JF002037

De Santis, F., Coviello, V., Manconi, A., Picozzi, M., & Godio, A. (2016). Characterization of mass movements in the Italian Alps using regional seismic networks. In *Proceedings of the 12Th International Symposium on Landslides, CRC Press, Napoli* (pp. 771–780).

Deparis, J., Jongmans, D., Cotton, F., Baillet, L., Thouvenot, F., & Hantz, D. (2008). Analysis of rock-fall and rock-fall avalanche seismograms in the French Alps. *Bulletin of the Seismological Society of America*, *98*(4), 1781–1796.

Eissler, H. K., & Kanamori, H. (1987). A single-force model for the 1975 Kalapana, Hawaii, earthquake. *Journal of Geophysical Research*, *92*(B6), 4827–4836.

Ekström, G., & Stark, C. P. (2013). Simple scaling of catastrophic landslide dynamics. *Science*, *339*(6126), 1416–1419.

Farin, M., Mangeney, A., De Rosny, J., Toussaint, R., Sainte-Marie, J., & Shapiro, N. M. (2016). Experimental validation of theoretical methods to estimate the energy radiated by elastic waves during an impact. *Journal of Sound and Vibration*, *362*, 176–202. https://doi.org/10.1016/j.jsv.2015.10.003

Farin, M., Mangeney, A., Toussaint, R., Rosny, J. D., Shapiro, N., Dewez, T., et al. (2015). Characterization of rockfalls from seismic signal: Insights from laboratory experiments. *Journal of Geophysical Research: Solid Earth*, *120*, 7102–7137. https://doi.org/10.1002/2015JB012331

Favreau, P., Mangeney, A., Lucas, A., Crosta, G., & Bouchut, F. (2010). Numerical modeling of landquakes. *Geophysical Research Letters*, *37*, L15305. https://doi.org/10.1029/2010GL043512

Giacomini, A., Buzzi, O., Renard, B., & Giani, G. (2009). Experimental studies on fragmentation of rock falls on impact with rock surfaces. *International Journal of Rock Mechanics and Mining Sciences*, *46*(4), 708–715.

Gili, J., Matas, G., Corominas, J., Núñez, M., Lantada, N., Ruiz-Carulla, R., et al. (2017). (2017, In Spanish), diseño y primeros resultados de tres ensayos de lanzamiento de bloques de roca para el estudio de la fragmentación. *TALUDES IX Simposio Nacional Sobre Taludes Y Laderas Inestables, 27–30 Junio 2017, Santander, España* (pp. 857–868).

Gili, J., Ruiz-Carulla, R., Matas, G., Corominas, J., Lantada, N., Núñez, M., et al. (2016). Experimental study on rockfall fragmentation: In situ test design and first results. In *International Symposium Landslides 2016 (ISL 2016)* (pp. 983–990). Naples, Italy: CRC Press/Balkema. https://doi.org/10.1201/b21520-116

Hartley, R., & Zisserman, A. (2003). *Multiple view geometry in computer vision*. Cambridge, UK: Cambridge University Press.

Helmstetter, A., & Garambois, S. (2010). Seismic monitoring of séchilienne rockslide (French Alps): Analysis of seismic signals and their correlation with rainfalls. *Journal of Geophysical Research*, *115*, F03016. https://doi.org/10.1029/2009JF001532

Hibert, C., Ekström, G., & Stark, C. (2017). The relationship between bulk-mass momentum and short-period seismic radiation in catastrophic landslides. *Journal of Geophysical Research: Earth Surface*, *122*, 1201–1215. https://doi.org/10.1002/2016JF004027

Hibert, C., Grandjean, G., Bitri, A., Travelletti, J., & Malet, J.-P. (2012). Characterizing landslides through geophysical data fusion: Example of the La Valette landslide (France). *Engineering Geology*, *128*, 23–29.

Hibert, C., Malet, J.-P., Bourrier, F., Provost, F., Berger, F., Bornemann, P., et al. (2017). Single-block rockfall dynamics inferred from seismic signal analysis. *Earth Surface Dynamics*, *5*, 283–292. https://doi.org/10.5194/esurf-5-283-2017

Hibert, C., Mangeney, A., Grandjean, G., Baillard, C., Rivet, D., Shapiro, N. M., et al. (2014). Automated identification, location, and volume estimation of rockfalls at piton de la fournaise volcano. *Journal of Geophysical Research: Earth Surface*, *119*, 1082–1105. https://doi.org/10.1002/2013JF002970

Hibert, C., Mangeney, A., Grandjean, G., & Shapiro, N. (2011). Slope instabilities in dolomieu crater, Réunion Island: From seismic signals to rockfall characteristics. *Journal of Geophysical Research*, *116*, F04032. https://doi.org/10.1029/2011JF002038

Hibert, C., Stark, C., & Ekström, G. (2015). Dynamics of the Oso-steelhead landslide from broadband seismic analysis. *Natural Hazards and Earth System Sciences*, *15*(6), 1265–1273. https://doi.org/10.5194/nhess-15-1265-2015

Huang, C.-J., Yin, H.-Y., Chen, C.-Y., Yeh, C.-H., & Wang, C.-L. (2007). Ground vibrations produced by rock motions and debris flows. *Journal of Geophysical Research*, *112*, F02014. https://doi.org/10.1029/2005JF000437

Hunter, S. (1957). Energy absorbed by elastic waves during impact. *Journal of the Mechanics and Physics of Solids*, *5*(3), 162–171.

Jaboyedoff, M., Oppikofer, T., Abellán, A., Derron, M.-H., Loye, A., Metzger, R., & Pedrazzini, A. (2012). Use of lidar in landslide investigations: A review. *Natural Hazards*, *61*(1), 5–28.

Kanamori, H. (1977). The energy release in great earthquakes. *Journal of Geophysical Research*, *82*(20), 2981–2987.

Kanamori, H., & Given, J. W. (1982). Analysis of long-period seismic waves excited by the May 18, 1980, eruption of Mount St. Helens. A terrestrial monopole? *Journal of Geophysical Research*, *87*(B7), 5422–5432.

Kawakatsu, H. (1989). Centroid single force inversion of seismic waves generated by landslides. *Journal of Geophysical Research*, *94*(B9), 12,363–12,374.

Lacroix, P., & Helmstetter, A. (2011). Location of seismic signals associated with microearthquakes and rockfalls on the Séchilienne landslide, French Alps. *Bulletin of the Seismological Society of America*, *101*(1), 341–353.

Lamb, H. (1904). On the propagation of tremors over the surface of an elastic solid. *Philosophical Transactions of the Royal Society of London. Series A, Containing Papers of a Mathematical or Physical Character*, *203*, 1–42.

Levy, C., Jongmans, D., & Baillet, L. (2011). Analysis of seismic signals recorded on a prone-to-fall rock column (Vercors massif, French Alps). *Geophysical Journal International*, *186*(1), 296–310.

Levy, C., Mangeney, A., Bonilla, F., Hibert, C., Calder, E. S., & Smith, P. J. (2015). Friction weakening in granular flows deduced from seismic records at the Soufrière Hills Volcano, Montserrat. *Journal of Geophysical Research: Solid Earth*, *120*, 7536–7557. https://doi.org/10.1002/2015JB012151

Matas, G., Lantada, N., Corominas, J., Gili, J., Ruiz-Carulla, R., & Prades, A. (2017). RockGIS: A GIS-based model for the analysis of fragmentation in rockfalls. *Landslides*, *14*(5), 1565–1578. https://doi.org/10.1007/s10346-017-0818-7

Matas, G., Lantada, N., Corominas, J., & Gili, J. (2016). Simulation of rockfall fragmentation mechanism in a GIS-based tool. In *ISRM International Symposium. In Rock Mechanics & Rock Engineering: From the Past to the Future* (pp. 671–675). Cappadocia, Turkey: CRC Press.

McLaskey, G. C., & Glaser, S. D. (2010). Hertzian impact: Experimental study of the force pulse and resulting stress waves. *Journal of the Acoustical Society of America*, *128*(3), 1087–1096.

Moretti, L., Mangeney, A., Capdeville, Y., Stutzmann, E., Huggel, C., Schneider, D., & Bouchut, F. (2012). Numerical modeling of the mount steller landslide flow history and of the generated long period seismic waves. *Geophysical Research Letters*, *39*, L16402. https://doi.org/10.1029/2012GL052511

Norris, R. D. (1994). Seismicity of rockfalls and avalanches at three cascade range volcanoes: Implications for seismic detection of hazardous mass movements. *Bulletin of the Seismological Society of America*, *84*(6), 1925–1939.

Papoulis, A. (1962). *The Fourier integral and its applications* (pp. 318). New York: McGraw-Hill.

Petley, D. (2013). Global losses from landslides associated with dams and reservoirs. *Italian Journal of Engineering Geology and Environment*, *6*, 63–72.

Prades, A., Matas, G., Núñez Andrés, M., Buil, F., Lantada, N., & Corominas, J. (2017). Determination of rocky blocks trajectories in essays using videogrammetry. In *1st Congress in Geomatic Engineering (CIGEO)*, July 5-6, Valencia, Spain.

Reed, J. (1985). Energy losses due to elastic wave propagation during an elastic impact. *Journal of Physics D: Applied Physics*, *18*(12), 2329–2337.

Ruiz-Carulla, R., Corominas, J., & Mavrouli, O. (2015). A methodology to obtain the block size distribution of fragmental rockfall deposits. *Landslides*, *12*(4), 815–825. https://doi.org/10.1007/s10346-015-0600-7

Ruiz-Carulla, R., Corominas, J., & Mavrouli, O. (2016). A fractal fragmentation model for rockfalls. *Landslides*, *14*, 875–889. https://doi.org/10.1007/s10346-016-0773-8

Schneider, D., Bartelt, P., Caplan-Auerbach, J., Christen, M., Huggel, C., & McArdell, B. W. (2010). Insights into rock-ice avalanche dynamics by combined analysis of seismic recordings and a numerical avalanche model. *Journal of Geophysical Research*, *115*, F04026. https://doi.org/10.1029/2010JF001734

Senfaute, G., Duperret, A., & Lawrence, J. (2009). Micro-seismic precursory cracks prior to rock-fall on coastal chalk cliffs: A case study at mesnil-val, normandie, nw france. *Natural Hazards and Earth System Science*, *9*(5), 1625–1641.

Simmons, G. (1964). Velocity of shear waves in rocks to 10 kilobars, 1. *Journal of Geophysical Research*, *69*(6), 1123–1130.

Spillmann, T., Maurer, H., Green, A. G., Heincke, B., Willenberg, H., & Husen, S. (2007). Microseismic investigation of an unstable mountain slope in the Swiss Alps. *Journal of Geophysical Research*, *112*, B07301. https://doi.org/10.1029/2006JB004723

Stein, S., & Wysession, M. (2003). *An introduction to seismology, earthquakes, and Earth structure*. Oxford, UK: Blackwell Publishing.

Sturzenegger, M., & Stead, D. (2003). Close-range terrestrial digital photogrammetry and terrestrial laser scanning for discontinuity characterization on rock cuts. *Engineering Geology*, *106*(3), 163–182.

Suriñach, E., Vilajosana, I., Khazaradze, G., Biescas, B., Furdada, G., & Vilaplana, J. (2005). Seismic detection and characterization of landslides and other mass movements. *Natural Hazards and Earth System Science*, *5*(6), 791–798.

Tsai, V. C., Minchew, B., Lamb, M. P., & Ampuero, J.-P. (2012). A physical model for seismic noise generation from sediment transport in rivers. *Geophysical Research Letters*, *39*, L02404. https://doi.org/10.1029/2011GL050255

Vidale, J. E. (1986). Complex polarization analysis of particle motion. *Bulletin of the Seismological Society of America*, *76*(5), 1393–1405.

Vilajosana, I., Suriñach, G., Khazaradze, G., & Gauer, P. (2007). Snow avalanche energy estimation from seismic signal analysis. *Cold Regions Science and Technology*, *50*(1-3), 72–85.

Vilajosana, I., Surinach, E., Abellán, A., Khazaradze, G., Garcia, D., & Llosa, J. (2008). Rockfall induced seismic signals: Case study in Montserrat, Catalonia. *Natural Hazards and Earth System Science*, *8*(4), 805–812.

Walter, M., Arnhardt, C., & Joswig, M. (2012). Seismic monitoring of rockfalls, slide quakes, and fissure development at the super-sauze mudslide, French Alps. *Engineering Geology*, *128*, 12–22.

Weichert, D., Horner, R. B., & Evans, S. G. (1994). Seismic signatures of landslides: The 1990 Brenda Mine collapse and the 1965 Hope rockslides. *Bulletin of the Seismological Society of America*, *84*(5), 1523–1532.

Xia, J., Miller, R. D., Park, C. B., & Tian, G. (2002). Determining q of near-surface materials from Rayleigh waves. *Journal of Applied Geophysics*, *51*(2), 121–129.

Yamada, M., Matsushi, Y., Chigira, M., & Mori, J. (2012). Seismic recordings of landslides caused by Typhoon Talas (2011), Japan. *Geophysical Research Letters*, *39*, L13301. https://doi.org/10.1029/2012GL052174